

Quantifying productivity at landscape scale using remotely-sensed foliar traits and canopy structure

Daniel Wieczynski (✉ daniel.wieczynski@gmail.com)

Duke University <https://orcid.org/0000-0003-4090-2677>

Sandra Diaz

Universidad Nacional de Córdoba <https://orcid.org/0000-0003-0012-4612>

Sandra M. Duran

University of Alberta

Nikolaos Fyllas

University of the Aegean

Norma Salinas

Pontificia Universidad Catolica del Peru

Roberta Martin

Arizona State University

Alexander Shenkin

University of Oxford <https://orcid.org/0000-0003-2358-9367>

Miles Silman

Wake Forest University

Gregory Asner

Center for Global Discovery and Conservation Science, Arizona State University

Lisa P. Bentley

Sonoma State University

Yadvinder Malhi

University of Oxford <https://orcid.org/0000-0002-3503-4783>

Brian Enquist

University of Arizona

Van Savage

University of California

Article

Keywords: canopy structure, forests, net primary productivity, remote sensing canopy functional model

Posted Date: November 2nd, 2020

DOI: <https://doi.org/10.21203/rs.3.rs-98574/v1>

License:  This work is licensed under a Creative Commons Attribution 4.0 International License.

[Read Full License](#)

1 **TITLE:** Quantifying productivity at landscape scale using remotely-sensed foliar traits and
2 canopy structure

3

4 **AUTHORS:**

5 Daniel J. Wieczynski^{1,2*}, Sandra Díaz³, Sandra M. Duran⁴, Nikolaos M. Fyllas⁵, Norma Salinas⁶,
6 Roberta Martin⁷, Alexander Shenkin⁸, Miles Silman⁹, Gregory P. Asner⁷, Lisa Patrick Bentley¹⁰,
7 Yadvinder Malhi⁸, Brian J. Enquist^{4,11}, & Van M. Savage^{1,11}

8

9 **AFFILIATIONS:**

10

11 ¹ Department of Ecology and Evolutionary Biology, University of California, Los Angeles, 612
12 Charles E Young Drive South, Los Angeles, California 90095, USA

13 ² Department of Biology, Duke University, 130 Science Drive, Durham, NC 27708, USA

14 ³ Consejo Nacional de Investigaciones Científicas y Técnicas, Instituto Multidisciplinario de
15 Biología Vegetal (IMBIV) and Facultad de Ciencias Exactas, Físicas y Naturales, Universidad
16 Nacional de Córdoba, Córdoba, Casilla de Correo 495, 5000, Córdoba, Argentina

17 ⁴ Department of Ecology and Evolutionary Biology, University of Arizona, 1041 E Lowell St
18 Tucson, Arizona 85721, USA

19 ⁵ Biodiversity Conservation Laboratory, Department of Environment, University of the Aegean,
20 Mytilene, 81100, Greece

21 ⁶ Institute for the Sciences of Nature, Earth and Energy (INTE-PUCP), Pontifical Catholic
22 University of Peru. Av. Universitaria 1801, Lima 15088, Peru

23 ⁷ School for Geographical Sciences and Urban Planning and Center for Global Discovery and
24 Conservation Science, Arizona State University, Tempe, AZ 85281, USA

25 ⁸ Environmental Change Institute, School of Geography and the Environment, University of
26 Oxford, South Parks Road, Oxford, OX1 3QY, UK

27 ⁹ Department of Biology and Center for Energy, Environment, and Sustainability, Wake Forest
28 University, Winston-Salem, NC 27109, USA

29 ¹⁰ Department of Biology, Sonoma State University, 1801 E. Cotati Avenue, Rohnert Park, CA
30 94928, USA

31 ¹¹ Santa Fe Institute, 1399 Hyde Park Road, Santa Fe, New Mexico 87501, USA

32 * Corresponding author

33

34

35

36

37 **ABSTRACT**

38 Forests are integral to global carbon cycling but are threatened by anthropogenic degradation and
39 climate change. Assessing this global threat has been hindered by a lack of clear, flexible, and
40 easy-to-use productivity models along with a lack of functional trait and productivity data for
41 parameterizing and testing those models. Current productivity models are either extremely
42 complex—requiring up to hundreds of parameters, many sub-models, and considerable
43 computational expense—or rely on statistical trait-growth relationships that can be hard to
44 extrapolate to new systems or climates. Here we provide a simple alternative: a remote sensing
45 canopy functional model (RS-CFM) that uses remotely-sensed foliar traits and canopy structure
46 data to efficiently map productivity at high-resolution and large spatial scales. We test this model
47 by quantifying net primary productivity (NPP) at 0.01-ha resolution in 30,040 hectares of
48 Peruvian tropical rainforest along a 3,322-m Amazon-to-Andes elevation gradient. Our model
49 predicts local NPP and elevational shifts in NPP much more accurately and in greater detail than
50 a prominent alternative method—NASA’s MODIS NPP product. Furthermore, we show how
51 NPP estimates depend on light competition and identify the appropriate spatial resolution for
52 remote productivity estimation. Our framework opens up possibilities to fully harness remote
53 sensing data and reliably scale up from traits to map regional or global productivity in a more
54 direct, efficient, and cost-effective manner.

55

56

57

58

59

60 **MAIN**

61 Forests are essential to the earth's active carbon cycle^{1,2} but their future is uncertain under the
62 current threats of anthropogenic degradation and climate change, especially in the tropics³⁻⁶.
63 Accurately predicting the consequences of these global threats will require understanding how
64 plant functional traits scale up to influence whole forest productivity^{7,8}. Morphological,
65 architectural, and chemical traits—such as plant height, biomass, leaf area index (LAI), wood
66 density, leaf mass per unit area (LMA), and leaf foliar chemistry (nitrogen, phosphorus, and
67 carbon content)—directly influence individual plant growth rates and survival and, in turn, forest
68 productivity^{7,9-15}. In addition, the collection of functional traits expressed within forests varies
69 substantially with changes in geography and climate^{8,16-18}. Directly linking traits with plant
70 growth and mapping shifts in functional composition with changes in environmental conditions
71 are therefore crucial to uncovering the forces driving variation in carbon flux across space and
72 time.

73
74 Relationships between trait composition and ecosystem processes have been difficult to discern
75 for two main reasons. First, it is challenging to accurately and comprehensively measure the
76 functional composition of forests, especially at large spatial scales and remote or difficult-to-
77 sample locations¹⁹. Solving this problem is the great promise of remote sensing (RS)
78 technology—using airborne or satellite imaging to collect extensive, high-resolution data at
79 local, regional, or global scales²⁰⁻²⁶. Remote sensing has created a surge of information about the
80 functional characteristics of forests^{21,24,26,27}, leading to important ecological insights about foliar
81 chemistry^{28,29}, forest canopy structure^{30,31}, taxonomic and functional diversity³²⁻³⁶, biomass and
82 carbon stocks^{37,38}, and relationships between functional traits and productivity³⁹⁻⁴¹. These

83 discoveries have resulted in the current initiatives to integrate remotely-sensed functional trait
84 data with vegetation growth models⁴²⁻⁴⁵—for example, dynamic global vegetation models
85 (DGVMs) like LPJ-DGVM⁴⁶ and ED2⁴⁷—to better assess spatiotemporal variation in carbon
86 storage/flux across scales.

87
88 The second challenge is that many studies that relate remotely-sensed forest data to productivity
89 do so via either empirical (statistical) models—using proxies of plant growth like chlorophyll⁴⁸,
90 nitrogen³⁹, light use efficiency (LUE)⁴¹, or the normalized difference vegetation index
91 (NDVI)^{49,50}—or DGVMs and individual-based forest simulators that are complex, requiring
92 many parameters and substantial computational power and time^{44,45,51-53}. Extrapolating the
93 results of purely empirical models to new systems and climates can be hazardous because they
94 lack mechanistic linkages among traits, plant growth, and productivity. Instead, they rely on
95 statistical relationships between plant growth proxies and productivity within a given dataset^{42,45}.
96 DGVMs and forest simulators often require specialized expertise, extensive data inputs, or
97 special access⁵¹, making them hard to implement or reproduce for most researchers. In such
98 models, functional traits are rarely collected remotely and are usually coarsely represented as
99 plant functional types rather than species- or individual-level traits^{42,45,53}. Moreover, competition
100 for light is often only crudely incorporated^{44,53-55}.

101
102 Using simpler, more mechanistic growth models that utilize remotely-sensed functional trait data
103 is a complementary alternative to these two approaches that can provide a fundamental basis for
104 understanding which factors are most important for driving variation in productivity. These
105 factors can then be varied within models to estimate productivity in new systems or changes in

106 productivity with changes in climate or forest composition/structure. As a first step, Enquist et
107 al.⁹ derived a trait-based metabolic scaling model that can be used to estimate whole forest net
108 primary productivity (NPP) based on direct relationships between key functional traits and
109 growth rates in individual trees. Fyllas et al.¹¹ extended this model using data collected via
110 conventional ground-based field sampling methods. They found that the key to accurately
111 estimating shifts in forest productivity across elevations is accounting for variation in functional
112 traits and canopy structure (light competition)¹¹.

113

114 Here we introduce a new remote sensing canopy functional model (RS-CFM, Figure 1) that
115 overcomes both data and modeling challenges by merging remotely-sensed functional-trait and
116 canopy-structural data with an updated version of the mechanistic growth model outlined
117 above^{9,11}. The RS-CFM has notable advantages over previous approaches. Our model is flexible
118 enough to apply to virtually any region or climate because vegetation growth rates are rooted in
119 direct links between a few key plant traits and metabolism, rather than statistical trait-
120 productivity relationships or the imprecise demography of plant functional types. This means
121 that productivity can be easily quantified across large regions using the rapidly-growing
122 inventory of remotely-sensed functional data. The RS-CFM also uses a light competition
123 function that accounts for continuous variation in biomass and light throughout the canopy—
124 significantly outperforming alternative methods without vertical canopy structure. Finally, the
125 simplicity of the RS-CFM relative to previous approaches makes it faster, easier to manipulate
126 and explore parameter space, easier to clarify relationships between plant traits and productivity,
127 and more accessible such that any individual can run it using their own data on their own

128 computer (i.e., without a supercomputer). Taken together, these advances will facilitate more
129 accurate, higher-resolution productivity estimates at larger spatial scales and lower costs.

130

131 We use this framework to evaluate the effects of forest functional composition on variation in
132 NPP along a 3,322-m elevation gradient in Peru. Our study area spans a mean annual
133 temperature gradient of $\sim 15^{\circ}\text{C}$ from the lowland Amazonian rainforest to montane forest in the
134 high Andes. Originally established by the Andes Biodiversity and Ecosystem Research Group
135 (ABERG)⁵⁶, this site provides a uniquely rich dataset including ground-based NPP⁵⁷ and plant
136 functional trait^{36,57} measurements as well as airborne lidar and imaging spectroscopy^{36,58}. First,
137 we assess whether our model is able to accurately predict local productivity and elevation shifts
138 in productivity in nine focal forest plots (Plot-scale) by comparing our model results with
139 ground-based NPP measurements⁵⁷ and ground-based NPP estimates using a trait-based growth
140 model¹¹. We then extend this method to quantify NPP in 30,040 hectares of forest surrounding
141 the nine focal plots along this elevation gradient (Landscape-scale). Finally, we compare our
142 results with those from another well-known method that uses remote sensing data collected via
143 satellite and estimates productivity using empirical modeling—NASA’s moderate resolution
144 imaging spectroradiometer (MODIS) NPP product (MOD17A3v055)⁵⁰.

145

146 Our results demonstrate that remotely-sensed trait data can be reliably scaled up to predict
147 variation in NPP across environmental gradients. This opens up possibilities to take advantage of
148 a rapidly-growing inventory of remote data and fulfill the current need for models that quantify
149 productivity across regions in a more direct, efficient, and cost-effective manner⁴².

150

151 RESULTS

152 Our framework quantifies productivity through four basic steps (Figure 1, see Methods for
153 details). First, airborne remote sensing data were collected by the Global Airborne Observatory
154 using visible-to-shortwave infrared (VSWIR) spectrometry and dual-laser waveform light
155 detection and ranging (LiDAR)⁵⁸. Second, VSWIR images were processed and analyzed using
156 partial least squares regression to estimate average values of leaf mass per unit area (LMA), leaf
157 nitrogen and phosphorus content per unit area (N_{area} , P_{area}) for the vegetation within individual
158 RS pixels^{36,58}. LMA, N_{area} , and P_{area} were then used as inputs to calculate leaf photosynthetic
159 rates (A_L). For each pixel, LiDAR top-of-canopy height measurements and plot-aggregate
160 allometry^{59,60} were used to estimate total aboveground biomass and leaf-mass allometry¹¹ was
161 used to calculate total leaf biomass (M_L). Third, to account for vertical heterogeneity in canopy
162 biomass and light availability, individual pixels were divided vertically into 1-m slices, each of
163 which was assigned a unique value for leaf biomass and solar radiation based on vertical biomass
164 and light profiles calculated using ground data. Finally, using our mechanistic plant growth
165 model (RS-CFM), we calculated pixel-level growth rates (\dot{M}_{pixel}) by summing growth estimates
166 across all vertical slices within each pixel at 0.01ha, 1ha, and 100ha spatial resolutions. NPP was
167 then calculated as the average growth rate across all pixels within a given plot or elevation band.

168

169 We begin by comparing our RS-CFM NPP estimates with ground-based NPP measurements⁵⁷
170 and ground-based model NPP estimates¹¹. In general, we found very close agreement between
171 ground- and remote-based NPP (Figures 2&S1). At both the plot- and landscape-scales, our
172 model accurately predicts local (within-elevation) NPP as well as characteristic declines in NPP
173 with increasing elevation, including the leveling off of NPP at high elevations (Figure 2a&b).

174 The highest-resolution plot-scale NPP estimates (RS-CFM Plot 0.01ha) performed best (Figures
175 2a&S1, Table S1), exhibiting a root mean square deviation (RMSD) between measured and
176 predicted NPP of 1.02, lower than all other datasets, even ground-based model estimates (ground
177 model: RMSD=1.28). At the level of individual pixels, growth estimates (\dot{M}_{pixel}) from the RS
178 Plot 0.01ha dataset also performed best, deviating from ground-based NPP measurements by
179 only 0.26 MgC ha⁻¹ yr⁻¹ on average (Figure 2c, Table S1).

180
181 Interestingly, we found that NPP estimates are sensitive to the spatial scale and resolution of the
182 remote dataset being used. Within all focal plots/elevations, RS-CFM NPP estimates decline
183 with decreasing pixel resolution (Figure 2a&b, Table S1). This results in a systematic, downward
184 shift in NPP-elevation trends at lower resolutions, despite the shapes of these trends remaining
185 relatively unchanged. Higher-resolution (0.01ha) plot-scale data produced highly accurate NPP
186 estimates (RMSD=1.02) while lower-resolution data slightly underestimated productivity
187 (RMSD=1.59) (Figure 2a), suggesting that the accuracy of NPP estimates increases with pixel
188 resolution. However, at the landscape scale, intermediate resolution (1ha) NPP estimates are
189 actually closest to NPP measurements (RMSD=1.08) (Figure 2b). Because ground-based NPP
190 measurements were originally collected within the same nine focal plots as our plot-scale remote
191 data, we expect our plot-scale NPP estimates to be more representative of the ground-based NPP
192 measurements used in this study than landscape-scale estimates. Given the positive relationship
193 between pixel resolution and NPP estimate accuracy at the plot-scale, it is possible that higher-
194 resolution (0.01ha) landscape-scale NPP estimates are actually be most representative of overall
195 regional productivity. However, verifying this would require more extensive ground sampling
196 throughout the region.

197
198 We compared our approach with NASA's MODIS terrestrial NPP product, an easily accessible
199 alternative method for estimating NPP using remote sensing data. MODIS produces NPP
200 estimates by combining Fraction of Photosynthetically Active Radiation (FPAR) and Leaf Area
201 Index (LAI) data collected via satellite imagery at 1km (100ha) spatial resolution with
202 conversion efficiency estimates that vary with plant functional types and climatic conditions^{49,50}.
203 For this comparison, we extracted all MODIS NPP data overlapping with our entire airborne
204 dataset, providing total spatial coverage at the landscape scale. MODIS NPP estimates are
205 considerably higher on average than NPP and pixel growth estimates from our model (Figure
206 2b&d, Figure S1). This result is similar to previous findings that DGVMs also tend to
207 overestimate biomass⁶¹. MODIS NPP remains relatively constant across elevations except for a
208 dramatic decline at higher elevations, in contrast to gradual declines across all elevations seen at
209 all spatial scales and resolutions using our model (Figure 2b). Moreover, the sharp decline in
210 MODIS NPP estimates occurs exactly where NPP measurements and our model estimates show
211 a leveling off. Interestingly, MODIS NPP estimates were very similar to RS-CFM NPP at the
212 highest elevation studied here (3537m; Figure 2b), potentially due to the sparseness of the
213 canopy reducing vertical variation in light availability. At the level of individual pixels, MODIS
214 NPP values were substantially higher on average than measured NPP values, exhibiting a mean
215 pixel growth rate deviation of 8.88 MgC ha⁻¹ yr⁻¹ (Figure 2d). Similarly, MODIS NPP estimates
216 were also much higher on average than any of our airborne RS-CFM growth rate estimates. Even
217 at the highest pixel resolution tested here (100ha), RS-CFM estimates (RMSD=1.72) represent a
218 significant improvement over MODIS estimates (RMSD=8.31) (Table S1, Figure S1).
219

220 The RS-CFM revealed extensive, fine-scale variation in vegetation growth rates at the level of
221 individual pixels (\dot{M}_{pixel}). We calculated deviations between \dot{M}_{pixel} and associated NPP
222 measurements and pooled these data by spatial scale and resolution to examine the overall
223 accuracy and spread of \dot{M}_{pixel} values (Figure 2c&d). As with NPP estimates, mean pixel growth
224 rate deviations increased with pixel resolution. High-resolution (0.01ha) plot-scale \dot{M}_{pixel}
225 estimates performed best, exhibiting deviations from measured NPP that were only slightly
226 higher on average than those of ground-based NPP estimates ($\mu=0.26$ and $\mu=0.13$ MgC ha⁻¹ yr⁻¹,
227 respectively; Figure 2c). Landscape-scale \dot{M}_{pixel} estimates also performed well at both 0.01ha
228 and 1ha resolutions (average deviations of $\mu=0.61$ and $\mu=-0.50$ MgC ha⁻¹ yr⁻¹, respectively;
229 Figure 2d). Lower-resolution data resulted in the largest mean pixel growth rate deviations, but
230 this effect was less exaggerated at the landscape scale (Figure 2c&d). In fact, the mean deviation
231 in \dot{M}_{pixel} at 1ha resolution was much lower at the landscape-scale ($\mu=-0.50$) than at the plot-scale
232 ($\mu=-1.49$)—which was also reflected in the accuracy of associated NPP estimates (plot-scale
233 RMSD=1.59, landscape-scale RMSD=1.08; Table S1)—suggesting that lower resolution remote
234 data may only provide accurate growth/NPP estimates at larger spatial scales. Variation in \dot{M}_{pixel}
235 deviations also increased with pixel resolution and was substantially higher at the landscape
236 scale (Figure 2c&d, Table S1), corresponding to wider and more continuous distributions of
237 pixel-level trait values both within and across elevations (Figure S2&S3).

238

239 Although smaller pixels are subject to increased uncertainty due to inherent errors associated
240 with fine-scale remote sensing data, it has been shown that 1ha resolution remote data for carbon
241 density estimates exhibit 90% agreement with ground-based field estimates^{59,62}. Conversely,
242 functional richness increases with sampling area^{63–65}, meaning that lower resolution remote data

243 may underestimate trait variation by averaging over larger areas. Therefore, based on this
244 reasoning and our empirical results, we propose more generally that 1ha-resolution trait and
245 productivity estimates most accurately reflect the true variation in forests, even across different
246 forests and environments. Further evaluating how these opposing forces produce variation in
247 remote trait and productivity estimates will be an interesting area of future study.

248

249 At all scales and resolutions, variation in pixel growth rates is linked to variation in underlying
250 traits. We performed a multiple regression on the individual trait components of our growth
251 model—pixel-level mean LMA, N_{area} , P_{area} , A_L , and M_L —against \dot{M}_{pixel} values using
252 standardized coefficients to determine which traits had the largest impact on variation in growth
253 rates. At all spatial scales and resolutions, M_L , A_L , and LMA were the strongest predictors of
254 variance in \dot{M}_{pixel} while leaf nitrogen and phosphorus content were less influential (e.g.,
255 parameter estimates in the RS-CFM 0.01ha model were: LMA=-2.03, N_{area} =0.07, P_{area} =0.23,
256 A_L =2.69, and M_L =2.47, adjusted R^2 =0.92, $p < 10^{-5}$; see Table S2). Trait distributions also shift in
257 position and shape along the elevation gradient (Figures S2&S3), consistent with shifts reported
258 in previous research in this region^{11,36}. However, here we also found associated shifts in the
259 distributions of \dot{M}_{pixel} values across elevations (Figure S2). We summarized these shifts by
260 calculating the first four central moments of \dot{M}_{pixel} distributions and evaluating both linear and
261 polynomial (quadratic) regressions across elevation (Figure S3). Mean \dot{M}_{pixel} values (our
262 measure of NPP) decline significantly with increasing elevation at all spatial scales and
263 resolutions. Variance, skewness and kurtosis in \dot{M}_{pixel} distributions tend to increase with
264 elevation. However, evidence for shifts in these higher moments is somewhat limited, except
265 perhaps at the landscape scale.

266

267 One of the most crucial and challenging components of our model is the inclusion of vertical
268 heterogeneity in light availability (light competition) (Figure 3). Instead of using a single light
269 value for each pixel, our RS-CFM uses a straightforward method for distributing light
270 continuously throughout the canopy. In order to evaluate the importance of this component, we
271 compared our light model with two alternatives that assume no vertical light gradient. When
272 vertical light profiles are held constant and light is assumed to be fully available throughout the
273 canopy (i.e., no light competition), our model overestimates productivity (Figure 3, “No
274 shading”). However, if we assume that light availability is limited by shading—determined by
275 leaf area index (LAI)—but is not distributed continuously throughout the canopy (*as is true in*
276 *most current carbon models*⁵³), then productivity is substantially underestimated (Figure 3,
277 “Average shading”). Accounting for this vertical light gradient avoids the problems with both of
278 the limits above and also considerably improves NPP estimates, regardless of the scale or
279 resolution of remote sensing data (Figure 2). These results are consistent with previous findings¹¹
280 that light competition does indeed play an essential role in the distribution of tree growth rates
281 and estimates of overall forest productivity.

282

283 Estimating growth rates using remote sensing data allows us to create high-resolution
284 productivity maps across large regions at multiple spatial scales (Figure 4). At the plot scale, we
285 find remarkable fine-grain spatial heterogeneity in growth rate estimates both within and across
286 elevations (Figure 4a). Landscape-scale data reveal a strong elevation gradient in productivity as
287 well as substantial local variation around this trend (Figure 4b). Such maps provide precise
288 information about the spatial distributions of traits and vegetation growth, allowing us to more

289 accurately measure shifts in productivity with shifts in environmental conditions and to better
290 identify local and regional hotspots in functional diversity and primary production.

291

292 **DISCUSSION**

293 Here we combined remotely-sensed trait and canopy data with a mechanistic vegetation growth
294 model to accurately and efficiently estimate productivity across large regions and in remote or
295 difficult to sample locations. This method creates NPP maps (Figure 4) in a more
296 straightforward, efficient, and reliable manner than current alternative models (e.g., MODIS
297 NPP; see Figure 2). Our model also exposes fundamental links between traits, canopy structure,
298 and productivity across a broad temperature/elevation gradient, thus illuminating how trait-
299 environment relationships scale up to control ecosystem functioning. This information can be
300 used to better understand the forces governing community assembly, help predict shifts in the
301 composition and function of forests in the future, and inform management and conservation
302 efforts by identifying productivity hotspots at high-resolution.

303

304 Although a variety of modeling frameworks have been developed to evaluate primary production
305 at large spatial scales, the remote sensing canopy functional model (RS-CFM) presented here
306 breaks from previous approaches in important ways. First, our model explicitly links plant traits
307 with growth, providing a highly flexible framework that can be applied across systems. This is in
308 contrast to previous models that rely on statistical relationships between variables within a
309 particular dataset, making extrapolation and prediction either challenging or impossible^{42,44,45}.
310 Second, we incorporate spatial variation in functional composition by collecting trait information
311 directly from remote sensing data at high spatial resolution. Although other models (specifically

312 DGVMs) often include remotely-sensed climate data, they typically include functional variation
313 via established relationships between climate variables and plant functional types^{42,45}.

314

315 Most importantly, our model provides a simpler alternative—without extensive assumptions or
316 the computational demands of simulations—that provides highly accurate estimates of
317 productivity based on forest functional composition at a given point in time (i.e., without the
318 need for repeated flyovers⁶⁶). Indeed, on a personal laptop computer with 4 CPU cores, it takes
319 only about 30 seconds to estimate productivity for the entire region studied here (30,040 ha) at
320 1ha resolution. This computational efficiency, the mechanistic linkages among traits and
321 productivity, and the rich coverage of spatial data through remote sensing are the main
322 advantages of the RS-CFM.

323

324 In contrast, DGVMs involve many parameters—sometimes hundreds—that appear throughout
325 several different submodels and subroutines that make numerous assumptions about the
326 processes underlying productivity^{45,55}. Moreover, individual-based models track individual trees
327 in a spatially explicit manner that requires lots of information and memory^{45,51}. These
328 simulation-based models are also evaluated on very short timescales (e.g., hourly as in ED2⁴⁷)
329 and often require “spin-up” periods to equilibrate to initial forest conditions prior to analysis
330 (e.g., 1000 yrs in LPJ-DGVM⁴⁶). These models are attractive, largely because of their attention
331 to such details, but the level of detail comes at considerable computational expense. The question
332 is: Does the predictive ability and accuracy of these models justify their computational expense?
333 Indeed, how do we quantify such tradeoffs and what data are available to analyze them?

334

335 In addition, our framework is flexible and can be easily generalized by including information
336 from other regions beyond the specific choices and calculations we made here for Peruvian
337 tropical forests. For example, it will be interesting to extend the RS-CFM framework to
338 temperate regions—where functional richness is relatively low^{17,67}—or regions exhibiting strong
339 gradients in other environmental variables, like precipitation or vapor pressure. To estimate
340 biomass within pixels we use an aggregate allometry that relates biomass to canopy heights and
341 elevation specifically for the wet montane forests of southern Peru⁵⁹. However, allometric
342 relationships between canopy height and biomass are known to vary across regions^{59,68}, which
343 can be accommodated in our model by altering the underlying biomass allometry accordingly.
344 We also use vertical LAI and biomass profiles derived from ground data in the nine focal plots in
345 this study. These components may also vary with study area and well as the level of disturbance
346 present in a given forest, but could be accounted for by incorporating more sophisticated remote
347 sensing methods that directly measure vertical canopy biomass profiles^{60,69}. Additionally, our
348 model assumes that leaf photosynthetic rate depends on leaf functional traits (LMA, N, and P)
349 according to relationships previously established for this region¹¹. How these traits interact to
350 influence photosynthesis may also depend on various environmental factors—e.g., temperature
351 and precipitation—that also vary across space, although much of this variation is already
352 contained implicitly in shifts in trait distributions themselves. Nevertheless, incorporating
353 environmental variables as predictors of photosynthetic rate might improve productivity
354 estimation and create a more flexible framework that can be applied to many different systems
355 and extended to predict changes in productivity according to projected changes in climatic
356 conditions in the future.

357

358 Remote sensing technology shows great promise for evaluating spatial and temporal variation in
359 forest functional composition and productivity. The remote data used in this study were collected
360 from an aircraft. However, such instruments may soon be available aboard satellites, too, and
361 will be able to collect global-scale data in high-frequency time-series (e.g., as in NASA's
362 MODIS dataset^{49,50}). We argue that combining elements of our canopy functional model with
363 increasingly available airborne and satellite remote sensing data has the potential to greatly
364 improve the spatio-temporal acuity of productivity estimates. This information will be especially
365 useful when evaluating the consequences of natural and anthropogenic degradation for the global
366 carbon budget.

367

368 Climate change and deforestation are expected to alter the spatial distribution of functional traits
369 expressed within forests^{7,17}. Our framework provides a mechanistic basis for predicting large-
370 scale changes in ecosystem functioning as a result of these expected future disturbances. A first
371 step toward such predictions might be to analyze time-series of remote sensing trait data to
372 establish relationships between changes in functional composition and changes in climate,
373 natural disturbances, anthropogenic impacts, etc. This information can then be combined with
374 mechanistic, trait-based models like ours and extrapolated based on expected future
375 environmental shifts. Analyzing such changes using high-resolution trait and productivity maps
376 will help decode connections between forest composition and NPP, leading to stronger
377 predictions about climate-induced shifts in carbon dynamics, more precise identification of
378 productivity hotspots, and more effective management strategies in the future. In this way,
379 directly linking productivity with functional traits and forest structure will not only improve our

380 ability to predict future changes, but will also lead to a deeper understanding of the basic
381 processes driving large-scale patterns in carbon dynamics within and across ecosystems.

382

383 **METHODS**

384 **Ground-based NPP measurements and estimates**

385 Our ground-based dataset consists of nine 1-ha forest plots situated along a 3322-meter Amazon
386 to Andes elevation transect in Peru established by the Andes Biodiversity and Ecosystem
387 Research Group (ABERG; <https://www.andesconservation.org/>) and incorporated into the Global
388 Ecosystems Monitoring (GEM) network and the “Challenging Attempt to Measure Biotic
389 Attributes along the Slope of the Andes” (CHAMBASA) project
390 (<http://gem.tropicalforests.ox.ac.uk/subprojects/traits-leaf-traits-colle>). Data collection methods
391 and ground-based NPP measurements and model estimates are described in detail in the original
392 articles and are summarized here. Ground-based NPP was originally measured and reported by
393 Malhi et al.⁵⁷ for all nine focal plots in the current study. Overall NPP was calculated as an
394 aggregate of multiple key components of the autotrophic carbon cycle, including canopy
395 litterfall, leaf loss to herbivory, aboveground woody productivity, and branch turnover.

396

397 Fyllas et al.¹¹ calculated ground-based NPP estimates with trait data collected using conventional
398 field measurements of individual trees (no remote sensing data). Within each plot, species
399 identity was determined for all stems greater than 10cm in diameter at breast height (DBH). For
400 a subset of these individual stems (~7%), wood density (WD), leaf dry mass per unit wet area
401 (LMA), leaf nitrogen (N) and phosphorus (P) content per unit area. These data were then

402 incorporated into an individual-based forest simulator to estimate NPP that uses the same
403 vegetation growth equation as in the current study.

404

405 Here we estimated ground-based NPP using the functional trait dataset from Fyllas et al.¹¹ and an
406 updated version of their original vegetation growth modeling framework. NPP (MgC ha⁻¹ yr⁻¹)
407 was calculated for each plot by calculating and summing the growth rates of all individual trees
408 within that plot:

$$409 \quad NPP = \sum \dot{M}_{tree}$$

410 where \dot{M}_{tree} is the whole-plant net biomass growth rate of an individual tree and was calculated
411 based on functional traits using an equation derived by Enquist et al.⁹:

$$412 \quad \dot{M}_{tree} = \frac{dM_{tree}}{dt} = \left(\frac{c}{\omega}\right) \left(\frac{1}{LMA}\right) A_L M_L$$

413 where c is carbon use efficiency and was previously observed to be constant throughout the
414 study region⁵⁷ ($c=0.33$, no units), ω is the whole-plant carbon mass fraction ($\omega=0.5$, no units), A_L
415 is leaf area specific photosynthetic rate (gC m⁻² y⁻¹), LMA is leaf mass per unit area (g/cm²), and
416 M_L is the total aboveground biomass of an individual tree that is allocated to leaves (kg). We
417 calculated total leaf biomass per tree (M_L) using allometric scaling¹¹:

$$418 \quad M_L = 0.158 * AGB^{0.707}$$

419 where total aboveground biomass per tree (AGB) is given by Chave et al.⁶⁸:

$$420 \quad AGB = 0.0673(WD * DBH^2 * H)^{0.976}$$

421 where WD is wood density, DBH is diameter at breast height, and H is whole tree height. H was
422 estimated for each tree using¹¹:

$$423 \quad H = \exp(1.51 + \log_{10}(DBH)^{0.84})$$

424 Net leaf photosynthetic rate (A_l) follows a Michaelis–Menten function¹¹:

$$425 \quad A_{net} = \frac{A_{max} I_{comp}}{k + I_{comp}} - R_d$$

426 where A_{net} is net leaf photosynthetic rate ($\mu\text{mol m}^{-2}\text{s}^{-1}$), A_{max} is the maximum photosynthetic rate
427 ($A_{max} = 12.13$), I_{comp} is irradiance available to each tree after accounting for light extinction (due
428 to light competition among trees), k is the half saturation constant of the photosynthetic light
429 response, and R_d is respiration in the light. The total leaf photosynthetic rate (A_L) was calculated
430 by dividing A_{net} by $12\text{h}/24\text{h}=0.5$ to account for day length, which is roughly invariant at these
431 near-equatorial latitudes. All photosynthesis parameters are in $\mu\text{mol m}^{-2}\text{s}^{-1}$. For each tree, A_{max} , k ,
432 and R_d were each calculated as functions of LMA (g m^{-2}), N_{area} (g m^{-2}), and P_{area} (g m^{-2})
433 according to parameters from an updated version of the multiple linear regression model given
434 by Fyllas et al.¹¹:

$$435 \quad \begin{aligned} A_{max} &= 10.25 + P * 15.51 \\ k &= 175.51 - 0.612 * LMA - 104.53 * N + 1412.23 * P + 0.785 * LMA * N - 8.395 * LMA * P \\ R_d &= -1.004 + 0.017 * LMA + 2.363 * N - 16.41 * P - 0.015 * LMA * N + 0.133 * LMA * P \end{aligned}$$

436

437 The solar irradiance available to each tree after accounting for canopy light extinction (I_{comp}) is
438 calculated as:

$$439 \quad I_{comp} = I * e^{(-0.5 * LAI_L)}$$

440 Total irradiance (I) was calculated by first converting total solar radiation measured for each
441 plot¹¹ (S in $\text{GJ m}^{-2} \text{y}^{-1}$) to photosynthetic photon flux density (PPFD) assuming a 0.48
442 photosynthetically active radiation (PAR) to solar short-wave radiation ratio, a total solar
443 radiation to PAR conversion factor of $4.6 \mu\text{mol J}^{-1}$, a total foliage absorbance factor assumed to
444 be 0.75^{70} , and a $\text{GJ m}^{-2} \text{y}^{-1}$ to $\text{J m}^{-2}\text{s}^{-1}$ conversion factor of 31.7 ($3.171\text{e}8 \text{ s/yr} * 1\text{e}9 \text{ J/GJ}$). Thus,
445 total irradiance was calculated as $I=S*0.48*4.6*0.75*31.7$. Then, light competition was

446 accounted for according to the Perfect Plasticity Approximation (PPA)⁵², in which the whole
447 canopy is divided into layers that receive some fraction of total solar radiation according to their
448 position in the canopy. Trees are sorted into layers by first estimating the crown area (C_A) of
449 each tree using¹¹:

$$450 \quad C_A = 0.696 * DBH^{1.305}$$

451 All trees within each plot were arranged in descending order according to height and their crown
452 areas were summed until the cumulative crown area equalled the total plot area¹¹. The height of
453 the last tree in this summation was determined to be the so-called ‘critical height’ for layer one
454 ($Z_{L=1}^*$). Trees taller than $Z_{L=1}^*$ receive full solar radiation, which was measured daily for each plot
455 and averaged over the course of one full year¹¹. Then, beginning with then next tallest tree below
456 this critical height, the process is repeated to determine the critical heights for layers 2, 3, and so
457 on until all trees are accounted for. Trees with height between $Z_{L=1}^*$ and $Z_{L=2}^*$, are shaded by the
458 first layer and so on according to Beer’s light extinction model with an extinction coefficient
459 $K=0.5$. The leaf area index for each canopy layer (LAI_L) was calculated as

$$460 \quad LAI_L = \frac{\sum F_A}{P_A} * (1 - L)$$

461 where $\sum F_A$ is the sum of the foliage areas of all trees within a canopy layer, P_A is plot ground
462 area, and L is the canopy layer.

463

464 For comparison between ground and RS-CFM growth rate estimates (Figure 2c), each 1ha
465 ground plot is considered to be a single 1ha ‘pixel’.

466

467 **Remote sensing Canopy Functional Model (RS-CFM) NPP estimation**

468 Visible-to-shortwave infrared (VSWIR) spectrometry and dual-laser waveform light detection
469 and ranging (LiDAR) data were collected remotely for the 9 focal plots by the Global Airborne
470 Observatory⁵⁸. Each remote sensing (RS) plot is geographically centered over its associated
471 ground plot and is 9ha in size. The raw hyperspectral and lidar data were processed to provide
472 estimates of mean top of canopy height (TCH), LMA, N, and P within 10m² pixels (0.01ha)
473 using a previously developed protocol^{28,36,58}. Hyperspectral data were shade-masked such that
474 only sunlit portions of the canopies were used to measure spectral profiles. RS trait data were
475 also collected for 30,040 hectares of forest surrounding the 9 focal RS plots. Each landscape-
476 scale RS pixel was assigned to an associated focal plot/elevation according to whichever focal
477 plot was nearest in elevation, creating exclusive elevation bands across the 3344m gradient.
478 0.01ha RS data were aggregated at 1ha resolution for both plot-scale and landscape scale
479 datasets. Additionally, landscape-scale RS data were aggregated at 100ha resolution for direct
480 comparison with NASA MODIS NPP estimates.

481
482 To account for vertical variation in biomass and light availability within remote sensing pixels,
483 we divided each RS pixel into horizontal slices 1m in height. Aboveground biomass and solar
484 radiation were then distributed to each slice according functions generated using ground plot data
485 (see below). Because of differences in the methods of height estimation using ground and RS
486 data, height values for all trees (ground data) and RS pixels were converted to their respective
487 height quantiles (H_{quantile}), thus allowing us to directly compare the vertical biomass and light
488 profiles of ground and RS data. We also removed any RS pixels with heights that were lower
489 than the minimum tree height available for each associated ground-based focal plot: 9m for

490 SPD_01; 10m for ACJ_01, ESP_01, TRU_04, WAY_01; 12m for PAN_02, SPD_01, TAM_05;
491 and 13m for TAM_06.

492

493 First, total biomass within each pixel was estimated as a function of top of canopy height (TCH)
494 using plot-aggregate allometric scaling^{59,60}. Total aboveground carbon density (ACD) within an
495 RS pixel is given by⁵⁹:

$$496 \quad ACD = 3.8358 * TCH^{0.2807} * BA^{0.9721} * WD^{1.3763}$$

497 where BA is the total basal area of all trees within a pixel and is also a function of TCH ⁵⁹:

$$498 \quad BA = 1.5056 * TCH$$

499 and WD is average wood density within a pixel which is a function of TCH ⁵⁹ and elevation
500 ($Elev$)⁷¹:

$$501 \quad WD = \begin{cases} 0.5881 - 0.0037 * TCH, & Elev \leq 400 \\ 0.5881 - 0.0037 * TCH + ((Elev - 400) * 0.00005), & Elev > 400 \end{cases}$$

502 ACD was converted into total aboveground biomass (AGB) by dividing ACD by the whole-plant
503 carbon mass fraction ($\omega=0.48$ ^{59,72}):

$$504 \quad AGB_{pixel} = ACD_{pixel} / \omega$$

505 Total leaf biomass was estimated for each pixel ($M_{L,pixel}$) by calculating the fraction of total AGB
506 that is leaf biomass (leaf mass fraction = $LMF = M_{L,pixel} / AGB$) within each ground plot and
507 multiplying by the AGB of each pixel in associated RS plots.

508

509 $M_{L,pixel}$ was then distributed across 1m slices within each RS pixel according the vertical
510 distribution of leaf biomass in ground plots. Ground-based vertical leaf biomass distributions
511 were calculated for each ground plot by arranging all trees by height within each plot and
512 calculating the cumulative distribution of leaf biomass across all tree heights (remembering that

513 these have been converted to height quantiles). For the i th slice within each pixel, leaf biomass
514 ($M_{L,i}$) was determined by calculating the cumulative leaf biomass up to the height quantile of that
515 slice ($H_{quantile,i}$) and subtracting the cumulative leaf biomass for the slice immediately below the
516 i th slice within that pixel ($i-1$).

517

518 Light availability was also distributed across slices within each RS pixel based on the vertical
519 distribution of solar radiation previously calculated for each ground plot. First, LAI_L values were
520 calculated as in the ground plots but using an allometric equation from Feldpausch et al.⁷³ that
521 estimates tree height as a function of diameter at breast height (DBH) and accounts for variation
522 in plot-level basal area (BA) and mean annual temperature (MAT) across plots (model variant:
523 region-environment-structure (West Amazonia)). Individual tree heights were calculated using
524 individual-level DBH values and plot-level BA and MAT ⁵⁷ values. For each plot, trees were
525 sorted by height and an exponential decay model was fit to the LAI_L values across all trees, thus
526 allowing us to calculate LAI for each RS slice as a continuous function across all heights with
527 parameter values that are unique to each plot/elevation:

$$528 \quad LAI_{slice} = Asym + (R_0 - Asym) * \exp(-rc * H_{quantile,adj})$$

529 where $Asym$ is the horizontal asymptote, R_0 is the y-intercept, rc is the rate constant, and
530 $H_{quantile,adj}$ is the height of the RS slice adjusted such that all RS pixels receive full light at the top
531 (maximum irradiance values varied with elevation according to Fyllas et al.¹¹) and light decays
532 with increasing LAI at the same rate in each pixel regardless of pixel height. $H_{quantile,adj}$ therefore
533 adjusts the original height of each RS pixel slice (H_{slice}) such that the top of canopy height for a
534 given pixel (TCH_{pixel}) matches the maximum top of canopy height for a given plot/elevation
535 ($TCH_{plot/elev}$):

536
$$H_{quantile,adj} = (TCH_{plot/elev} - TCH_{pixel} + H_{slice})/TCH_{plot/elev}$$

537

538 In order to evaluate the effect of light availability on NPP predictions, we tested the above model
 539 of continuous light extinction against two alternative models without vertical heterogeneity in
 540 light availability. For the “average shading” version of the model (Figure 3), we calculated the
 541 average *LAI* across all slices within each individual pixel and assigned this average value to all
 542 slices within that pixel. For the “no shading” version of the model, we simply set all *LAI* values
 543 to 0, effectively eliminating all shading and allowing full light throughout the canopy.

544

545 The rate of change in biomass over time for each pixel slice was calculated using the mean trait
 546 values available for each RS pixel (same values used for each slice within a pixel):

547
$$\frac{dM_{slice}}{dt} = \left(\frac{c}{\omega}\right) \left(\frac{1}{LMA}\right) A_{L,slice} M_{L,slice}$$

548 and total growth rate per pixel is the sum of growth across all slices within that pixel:

549
$$\dot{M}_{pixel} = \frac{dM_{pixel}}{dt} = \sum \frac{dM_{slice}}{dt}$$

550 Finally, total annual plot NPP was calculated by taking the mean value of \dot{M}_{pixel} across all RS
 551 pixels associated with a given plot/elevation:

552
$$NPP = \frac{1}{n} \sum \dot{M}_{pixel}$$

553 The units for both \dot{M}_{pixel} and NPP were standardized to MgC ha⁻¹ yr⁻¹ at all spatial scales and
 554 resolutions to enable cross-comparison.

555

556 To compare our method to an alternative method of estimating NPP using RS data, we collected
 557 NPP estimates from NASA’s moderate resolution imaging spectroradiometer (MODIS)

558 terrestrial NPP product (MOD17A3v055)^{49,50}. Detailed information about methods of collection,
559 NPP calculation, and pre-analysis for MODIS data are available at the MODIS data website
560 (<https://modis.gsfc.nasa.gov/data/dataproduct/mod17.php>). We gathered all unique MODIS NPP
561 pixels overlapping with our 0.01ha-resolution airborne RS data. MODIS pixels overlapping with
562 airborne RS pixels in multiple elevation bands were added to each elevation for analysis.

563

564 **Trait and \dot{M}_{pixel} analyses**

565 Pixel growth rate deviations were calculated by subtracting the associated empirical NPP
566 measurements for a given focal plot/elevation from the RS-CFM model NPP estimates. In order
567 to compare NPP estimates from each dataset with empirically measured NPP, we calculated root
568 mean squared deviations (RMSD) between measured and estimated (predicted) NPP values for
569 each plot/elevation as:

$$570 \quad RMSD = \sqrt{E \left((NPP_{measured} - NPP_{predicted})^2 \right)}$$

571

572 where $E()$ represents the expected value. To differentiate the contributions of individual RS-
573 CFM growth model components—LMA, N_{area} , P_{area} , A_L , and M_L —on pixel-level growth rates
574 (\dot{M}_{pixel}) we performed a main effects multiple linear regression with standardized coefficients. To
575 produce standardized regression coefficients, we centered and rescaled all independent variables
576 (growth model components) prior to analysis by subtracting the means and dividing by their
577 standard deviations.

578

579 We evaluated shifts in the distributions of individual RS-CFM growth model components and
580 \dot{M}_{pixel} values by first calculating the first four central moments of each variable within each
581 plot/elevation:

$$582 \quad \text{Mean} = \mu_x = \frac{\sum x_i}{n}$$

583

$$584 \quad \text{Variance} = \sigma_x^2 = \frac{\sum (x_i - \mu_x)^2}{n}$$

585

$$586 \quad \text{Skewness} = \frac{\sum \left(\frac{x_i - \mu_x}{\sqrt{\sigma_x^2}} \right)^3}{n}$$

587

$$588 \quad \text{Kurtosis} = \frac{\sum \left(\frac{x_i - \mu_x}{\sqrt{\sigma_x^2}} \right)^4}{n} - 3$$

589

590 Relationships between the moments of each variable at each spatial scale and resolution were
591 then evaluated using both linear and quadratic regression analyses. In cases where both linear
592 and quadratic models produced significant fits and AIC scores differed by less than 4 points, the
593 linear model was chosen as the best fit model on the basis of parsimony (fewer parameters).

594

595 All data analyses and productivity estimations were performed in R version 4.0.0⁷⁴.

596

597 **ACKNOWLEDGMENTS**

598 This work was supported by NSF grant DEB1457812 (to B.J.E., L.P.B., G.P.A., and V.M.S.).

599 D.J.W. and V.M.S. were also supported by the James F. McDonnell Complex Systems Scholar

600 Award. This work is a product of the Global Ecosystems Monitoring (GEM) network

601 (gem.tropicalforests.ox.ac.uk), the Andes Biodiversity and Ecosystems Research Group ABERG

602 (andesresearch.org), and the Amazon Forest Inventory Network RAINFOR (www.rainfor.org)

603 research consortia. The field campaign was funded by grants to Y.M. from the UK Natural
604 Environment Research Council (Grant NE/J023418/1), with additional support from European
605 Research Council advanced investigator grants GEM-TRAITS (321131) and T-FORCES
606 (291585) under the European Union's Seventh Framework Programme (FP7/2007-2013). Plot
607 inventories were supported by funding from the US National Science Foundation Long-Term
608 Research in Environmental Biology program (LTREB; DEB 1754647) and the Gordon and Betty
609 Moore Foundation Andes-Amazon Program. We thank the Servicio Nacional de Áreas Naturales
610 Protegidas por el Estado (SERNANP) and personnel of Manu and Tambopata National Parks for
611 logistical assistance and permission to work in the protected areas. We also thank the Explorers'
612 Inn and the Pontifical Catholic University of Peru, as well as AmazonConservation/ACCA for
613 use of the Tambopata and Wayqecha Research Stations, respectively. We are indebted to
614 Professor Eric Cosio (Pontifical Catholic University of Peru) for assistance with research
615 permissions and sample analysis and storage. Taxonomic work at Carnegie Institution was
616 facilitated by Raul Tupayachi, Felipe Sinca, and Nestor Jaramillo. G.P.A. was supported by the
617 endowment of the Carnegie Institution for Science and a grant from the National Science
618 Foundation (DEB-1146206. Y. M. was also supported by the Jackson Foundation. B.J.E. was
619 also supported by NSF HDR-1934790. Finally, we thank the over 200 young Peruvian scientists
620 and students who have trained and worked tirelessly on this project over the years.

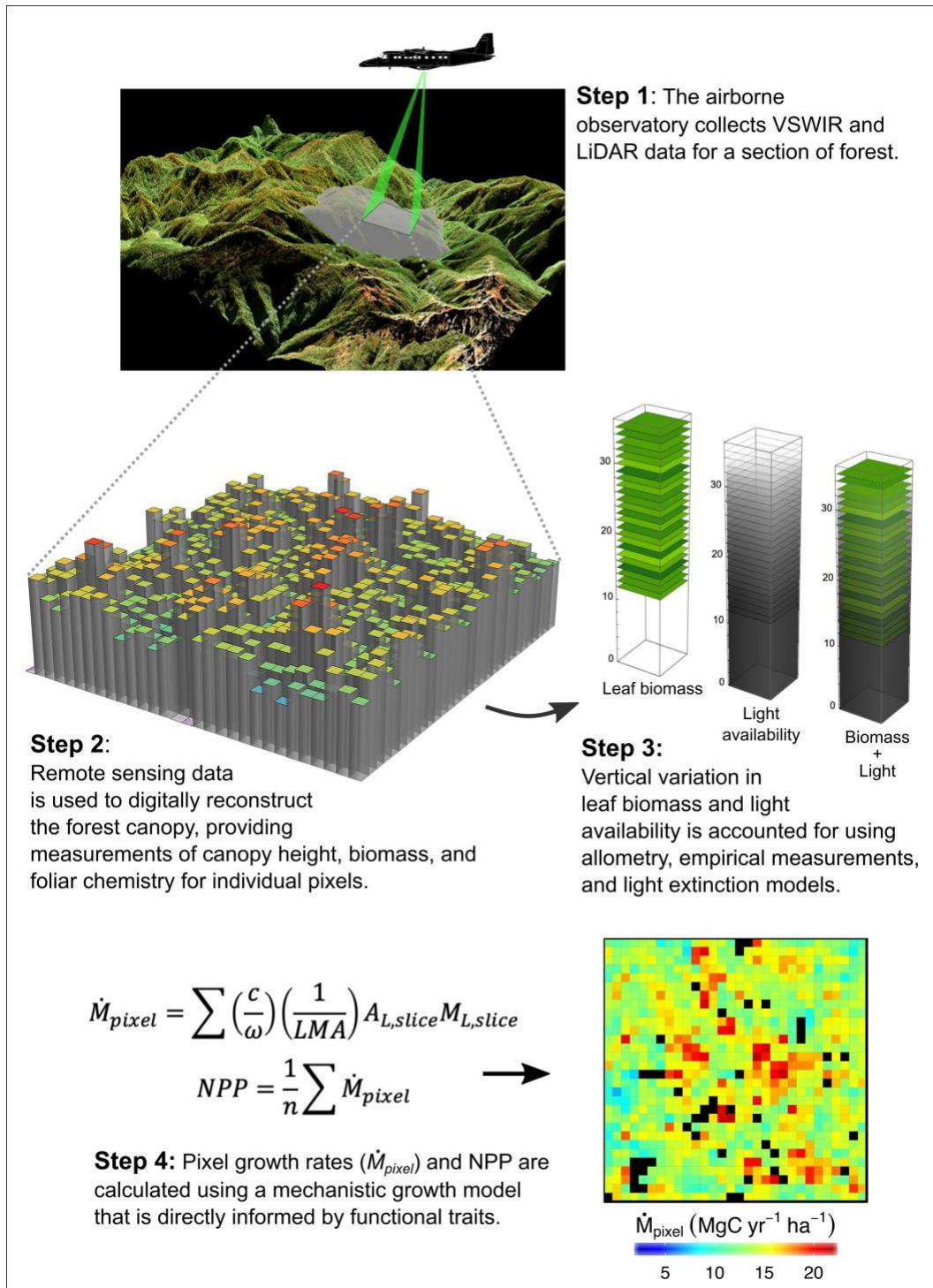
621

622

623

624

625



627

628 **Figure 1.** Step-by-step process for converting remote sensing data into productivity estimates

629 using our trait-based remote sensing canopy functional model (RS-CFM) framework. Growth

630 rate estimates for individual remote sensing pixels (\dot{M}_{pixel}) are based on key functional traits
631 including carbon use efficiency (c), carbon mass fraction (ω), leaf mass per unit area (LMA), leaf
632 photosynthetic rate (A_L)—which is a function of LMA and leaf nitrogen (N) and phosphorus (P)
633 content—and leaf biomass (M_L). Within each pixel, A_L and M_L are further subdivided into 1m
634 pixel slices to account for vertical gradients light and biomass throughout the canopy (Step 3).

635

636

637

638

639

640

641

642

643

644

645

646

647

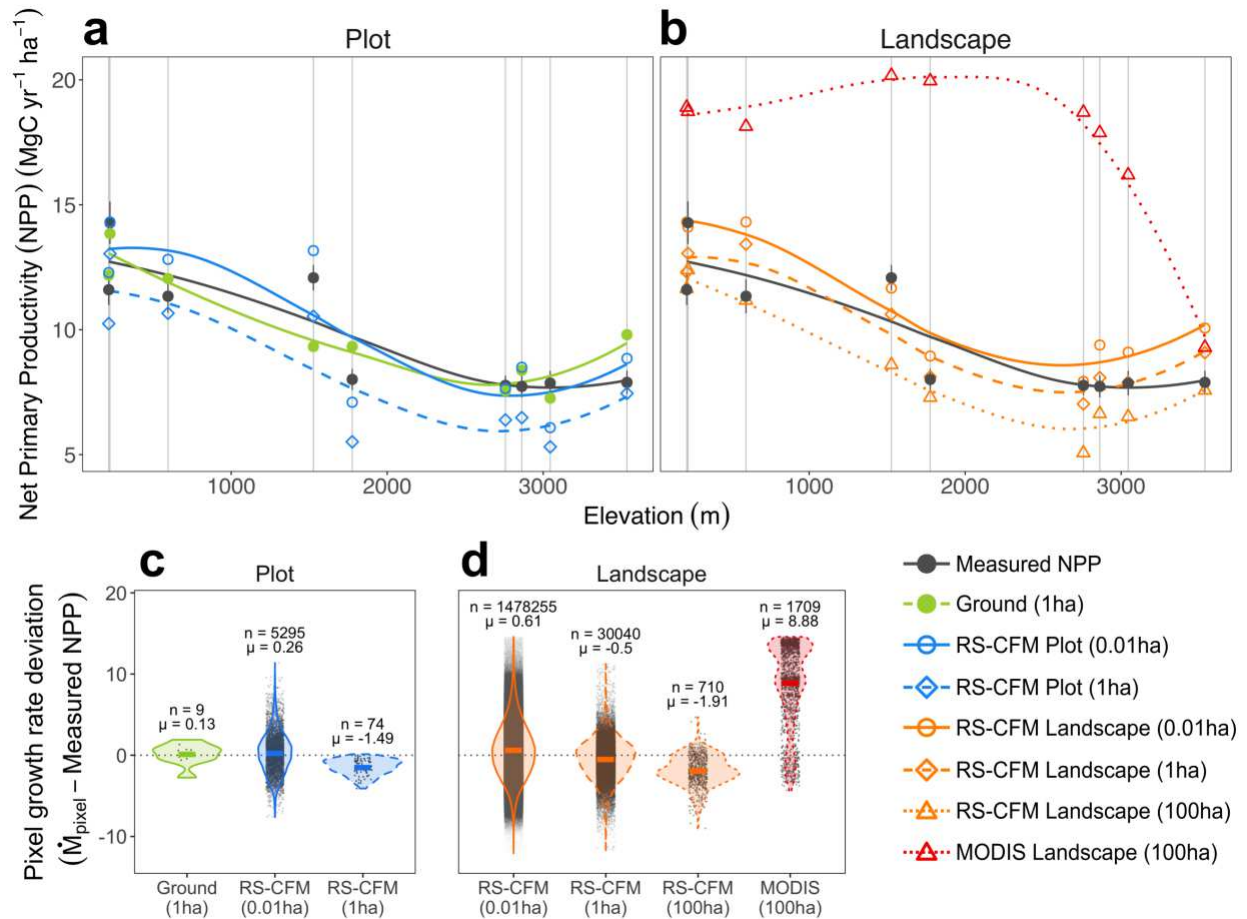
648

649

650

651

652



653

654 **Figure 2.** (a-b) Net primary productivity (NPP) and (c-d) individual pixel vegetation growth rate

655 estimates (\dot{M}_{pixel}) from ground-based, airborne remote sensing (RS-CFM), and NASA-MODIS

656 NPP models shown at multiple spatial scales (plot and landscape) and resolutions (0.01ha, 1ha,

657 and 100ha). NPP estimates are shown across elevations and compared with ground-based NPP

658 measurements (black) and ground-based NPP model estimates (green) at (a) plot- and (b)

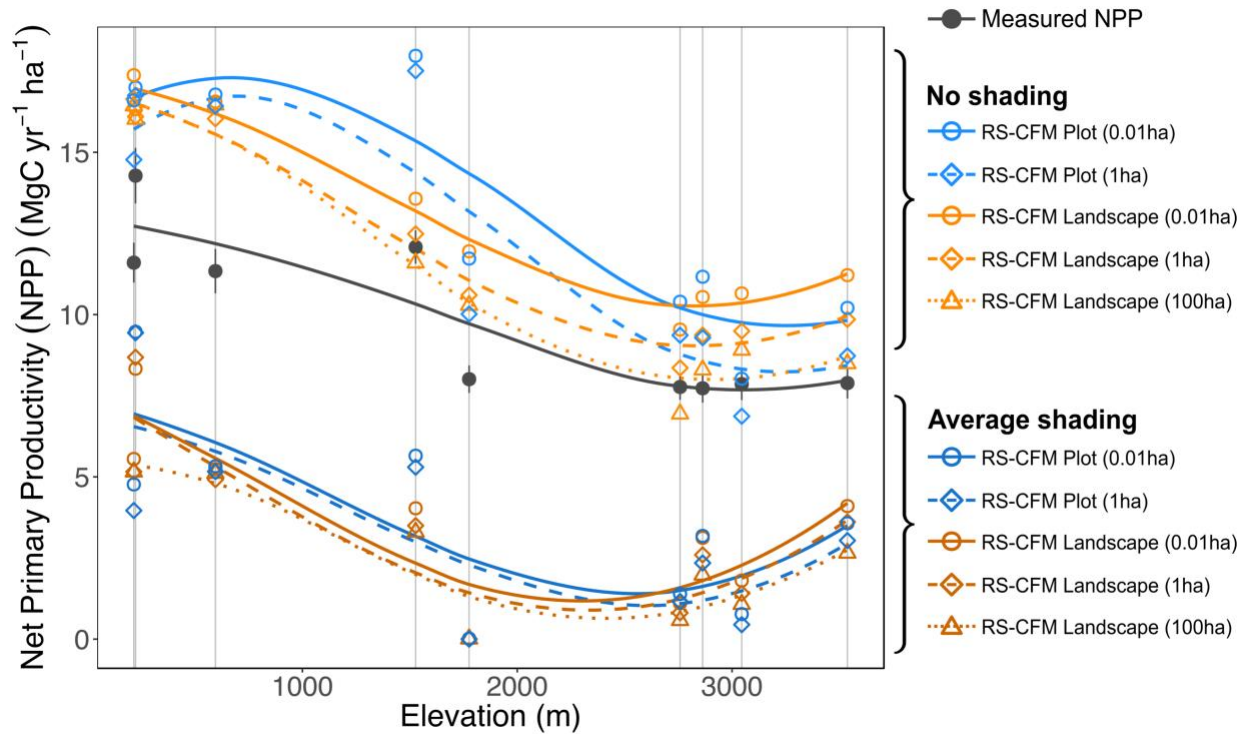
659 landscape-scales. Deviations between pixel growth rate estimates (\dot{M}_{pixel}) and NPP

660 measurements at (c) the plot scale and (d) landscape scales. Each gray dot represents the

661 deviation between an individual \dot{M}_{pixel} estimate and the empirical NPP measurement of its

662 associated focal plot and horizontal bars indicate mean values. Note how both mean and variance

663 in \dot{M}_{pixel} deviations tend to increase with increasing pixel resolution.



664

665 **Figure 3.** Remote sensing productivity estimates (RS-CFM) calculated using alternative canopy
 666 shading schemes. “No shading” indicates that light is freely available throughout the canopy and
 667 “Average shading” indicates that each vertical canopy slice receives the same amount of light
 668 equal to the average throughout a given pixel.

669

670

671

672

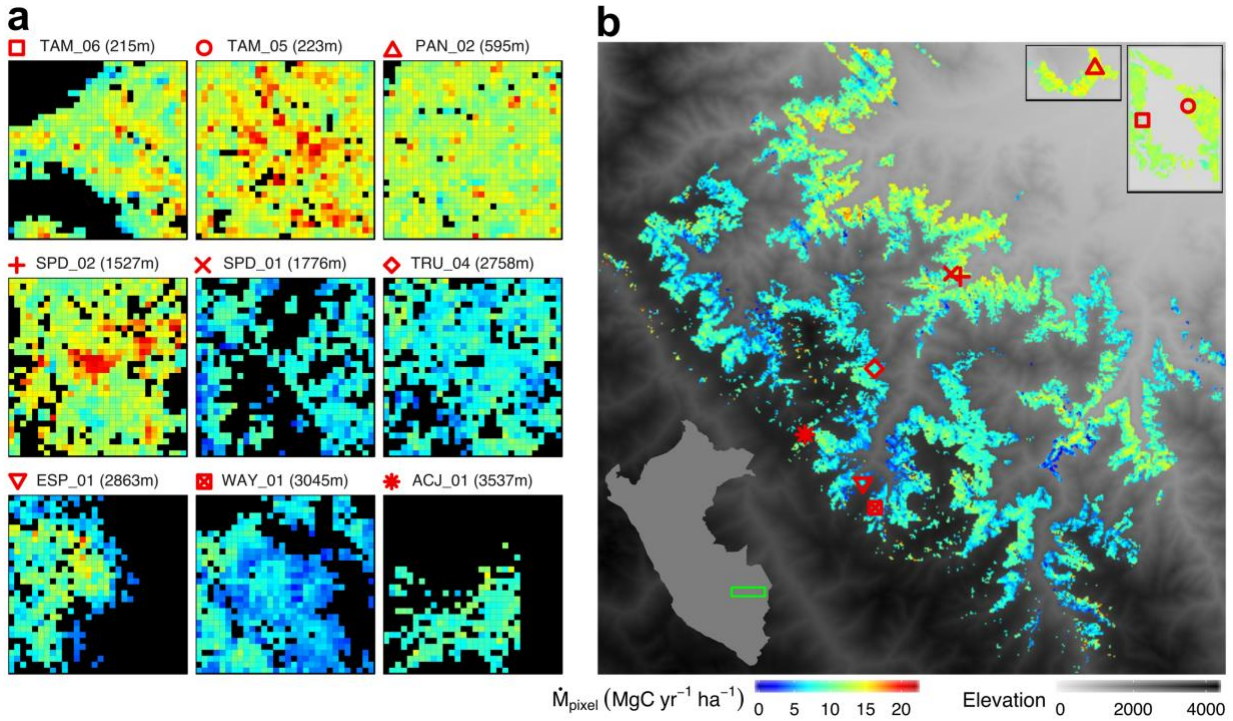
673

674

675

676

677



678

679 **Figure 4.** Spatial maps of landscape-scale growth estimates for individual pixels (\dot{M}_{pixel}) using
 680 our remote sensing canopy functional model (RS-CFM) at (a) 0.01ha resolution for individual
 681 forest plots and (b) 1ha-resolution for 30,040 hectares of forest surrounding the nine focal plots.
 682 Boxes in the upper right corner show areas outside the main plot area. Black pixels in plot-level
 683 images are no data values.

684

685

686

687

688

689

690

691

692 **References**

- 693 1. Field, C. B., Behrenfeld, M. J., Randerson, J. T. & Falkowski, P. Primary Production of the
694 Biosphere: Integrating Terrestrial and Oceanic Components. *Science* **281**, 237–240 (1998).
- 695 2. Pan, Y. *et al.* A Large and Persistent Carbon Sink in the World’s Forests. *Science* **333**, 988–
696 993 (2011).
- 697 3. Baccini, A. *et al.* Tropical forests are a net carbon source based on aboveground
698 measurements of gain and loss. *Science* **358**, 230–234 (2017).
- 699 4. Mitchard, E. T. A. The tropical forest carbon cycle and climate change. *Nature* **559**, 527–534
700 (2018).
- 701 5. Schimel, D., Stephens, B. B. & Fisher, J. B. Effect of increasing CO₂ on the terrestrial carbon
702 cycle. *Proc. Natl. Acad. Sci.* **112**, 436–441 (2015).
- 703 6. Grace, J., Mitchard, E. & Gloor, E. Perturbations in the carbon budget of the tropics. *Glob.*
704 *Change Biol.* **20**, 3238–3255 (2014).
- 705 7. Enquist, B. J. *et al.* Chapter Nine - Scaling from Traits to Ecosystems: Developing a General
706 Trait Driver Theory via Integrating Trait-Based and Metabolic Scaling Theories. in *Advances*
707 *in Ecological Research* (eds. Pawar, S., Woodward, G. & Dell, A. I.) vol. 52 249–318
708 (Academic Press, 2015).
- 709 8. Violle, C., Reich, P. B., Pacala, S. W., Enquist, B. J. & Kattge, J. The emergence and promise
710 of functional biogeography. *Proc. Natl. Acad. Sci.* **111**, 13690–13696 (2014).
- 711 9. Enquist, B. J. *et al.* A general integrative model for scaling plant growth, carbon flux, and
712 functional trait spectra. *Nature* **449**, 218–222 (2007).
- 713 10. Wright, I. J. *et al.* The worldwide leaf economics spectrum. *Nature* **428**, 821–827 (2004).

- 714 11. Fyllas, N. M. *et al.* Solar radiation and functional traits explain the decline of forest
715 primary productivity along a tropical elevation gradient. *Ecol. Lett.* **20**, 730–740 (2017).
- 716 12. Díaz, S. *et al.* The global spectrum of plant form and function. *Nature* **529**, 167–171
717 (2016).
- 718 13. Adler, P. B. *et al.* Functional traits explain variation in plant life history strategies. *Proc.*
719 *Natl. Acad. Sci.* **111**, 740–745 (2014).
- 720 14. Funk, J. L. *et al.* Revisiting the Holy Grail: using plant functional traits to understand
721 ecological processes. *Biol. Rev.* **92**, 1156–1173 (2017).
- 722 15. Violle, C. *et al.* Let the concept of trait be functional! *Oikos* **116**, 882–892 (2007).
- 723 16. Bruelheide, H. *et al.* Global trait–environment relationships of plant communities. *Nat.*
724 *Ecol. Evol.* **2**, 1906–1917 (2018).
- 725 17. Wieczynski, D. J. *et al.* Climate shapes and shifts functional biodiversity in forests
726 worldwide. *Proc. Natl. Acad. Sci.* **116**, 587–592 (2019).
- 727 18. Šímová, I. *et al.* Shifts in trait means and variances in North American tree assemblages:
728 species richness patterns are loosely related to the functional space. *Ecography* **38**, 649–658
729 (2015).
- 730 19. Newbold, T., Butchart, S. H. M., Şekercioğlu, Ç. H., Purves, D. W. & Scharlemann, J. P.
731 W. Mapping Functional Traits: Comparing Abundance and Presence-Absence Estimates at
732 Large Spatial Scales. *PLOS ONE* **7**, e44019 (2012).
- 733 20. Vane, G. & Goetz, A. F. H. Terrestrial imaging spectroscopy. *Remote Sens. Environ.* **24**,
734 1–29 (1988).
- 735 21. Aplin, P. Remote sensing: ecology. *Prog. Phys. Geogr. Earth Environ.* **29**, 104–113
736 (2005).

- 737 22. Ustin, S. L., Roberts, D. A., Gamon, J. A., Asner, G. P. & Green, R. O. Using Imaging
738 Spectroscopy to Study Ecosystem Processes and Properties. *BioScience* **54**, 523–534 (2004).
- 739 23. Green, R. O. *et al.* Imaging Spectroscopy and the Airborne Visible/Infrared Imaging
740 Spectrometer (AVIRIS). *Remote Sens. Environ.* **65**, 227–248 (1998).
- 741 24. Houborg, R., Fisher, J. B. & Skidmore, A. K. Advances in remote sensing of vegetation
742 function and traits. *Int. J. Appl. Earth Obs. Geoinformation* **43**, 1–6 (2015).
- 743 25. Gillespie, T. W., Foody, G. M., Rocchini, D., Giorgi, A. P. & Saatchi, S. Measuring and
744 modelling biodiversity from space. *Prog. Phys. Geogr. Earth Environ.* **32**, 203–221 (2008).
- 745 26. de Araujo Barbosa, C. C., Atkinson, P. M. & Dearing, J. A. Remote sensing of ecosystem
746 services: A systematic review. *Ecol. Indic.* **52**, 430–443 (2015).
- 747 27. Chambers, J. Q. *et al.* Regional ecosystem structure and function: ecological insights
748 from remote sensing of tropical forests. *Trends Ecol. Evol.* **22**, 414–423 (2007).
- 749 28. Asner, G. P. & Martin, R. E. Spectranomics: Emerging science and conservation
750 opportunities at the interface of biodiversity and remote sensing. *Glob. Ecol. Conserv.* **8**, 212–
751 219 (2016).
- 752 29. Lausch, A., Erasmi, S., King, D. J., Magdon, P. & Heurich, M. Understanding Forest
753 Health with Remote Sensing -Part I—A Review of Spectral Traits, Processes and Remote-
754 Sensing Characteristics. *Remote Sens.* **8**, 1029 (2016).
- 755 30. Lim, K., Treitz, P., Wulder, M., St-Onge, B. & Flood, M. LiDAR remote sensing of
756 forest structure. *Prog. Phys. Geogr. Earth Environ.* **27**, 88–106 (2003).
- 757 31. Zimble, D. A. *et al.* Characterizing vertical forest structure using small-footprint airborne
758 LiDAR. *Remote Sens. Environ.* **87**, 171–182 (2003).

- 759 32. Wang, R. & Gamon, J. A. Remote sensing of terrestrial plant biodiversity. *Remote Sens.*
760 *Environ.* **231**, 111218 (2019).
- 761 33. Nagendra, H. Using remote sensing to assess biodiversity. *Int. J. Remote Sens.* **22**, 2377–
762 2400 (2001).
- 763 34. Schneider, F. D. *et al.* Mapping functional diversity from remotely sensed morphological
764 and physiological forest traits. *Nat. Commun.* **8**, 1–12 (2017).
- 765 35. Durán, S. M. *et al.* Informing trait-based ecology by assessing remotely sensed functional
766 diversity across a broad tropical temperature gradient. *Sci. Adv.* **5**, eaaw8114 (2019).
- 767 36. Asner, G. P. *et al.* Scale dependence of canopy trait distributions along a tropical forest
768 elevation gradient. *New Phytol.* **214**, 973–988 (2017).
- 769 37. Goetz, S. & Dubayah, R. Advances in remote sensing technology and implications for
770 measuring and monitoring forest carbon stocks and change. *Carbon Manag.* **2**, 231–244
771 (2011).
- 772 38. Lu, D. The potential and challenge of remote sensing-based biomass estimation. *Int. J.*
773 *Remote Sens.* **27**, 1297–1328 (2006).
- 774 39. Smith, M.-L. *et al.* Direct estimation of aboveground forest productivity through
775 hyperspectral remote sensing of canopy nitrogen. *Ecol. Appl.* **12**, 1286–1302 (2002).
- 776 40. Song, C., Dannenberg, M. P. & Hwang, T. Optical remote sensing of terrestrial
777 ecosystem primary productivity. *Prog. Phys. Geogr. Earth Environ.* **37**, 834–854 (2013).
- 778 41. Hilker, T., Coops, N. C., Wulder, M. A., Black, T. A. & Guy, R. D. The use of remote
779 sensing in light use efficiency based models of gross primary production: A review of current
780 status and future requirements. *Sci. Total Environ.* **404**, 411–423 (2008).

- 781 42. Boisvenue, C. & White, J. C. Information Needs of Next-Generation Forest Carbon
782 Models: Opportunities for Remote Sensing Science. *Remote Sens.* **11**, 463 (2019).
- 783 43. Homolová, L., Malenovský, Z., Clevers, J. G. P. W., García-Santos, G. & Schaepman, M.
784 E. Review of optical-based remote sensing for plant trait mapping. *Ecol. Complex.* **15**, 1–16
785 (2013).
- 786 44. Scheiter, S., Langan, L. & Higgins, S. I. Next-generation dynamic global vegetation
787 models: learning from community ecology. *New Phytol.* **198**, 957–969 (2013).
- 788 45. Fisher, R. A. *et al.* Vegetation demographics in Earth System Models: A review of
789 progress and priorities. *Glob. Change Biol.* **24**, 35–54 (2018).
- 790 46. Sitch, S. *et al.* Evaluation of ecosystem dynamics, plant geography and terrestrial carbon
791 cycling in the LPJ dynamic global vegetation model. *Glob. Change Biol.* **9**, 161–185 (2003).
- 792 47. Medvigy, D., Wofsy, S. C., Munger, J. W., Hollinger, D. Y. & Moorcroft, P. R.
793 Mechanistic scaling of ecosystem function and dynamics in space and time: Ecosystem
794 Demography model version 2. *J. Geophys. Res. Biogeosciences* **114**, (2009).
- 795 48. Madani, N., Kimball, J. S., Jones, L. A., Parazoo, N. C. & Guan, K. Global Analysis of
796 Bioclimatic Controls on Ecosystem Productivity Using Satellite Observations of Solar-
797 Induced Chlorophyll Fluorescence. *Remote Sens.* **9**, 530 (2017).
- 798 49. Running, S. W. *et al.* A Continuous Satellite-Derived Measure of Global Terrestrial
799 Primary Production. *BioScience* **54**, 547–560 (2004).
- 800 50. Zhao, M., Heinsch, F. A., Nemani, R. R. & Running, S. W. Improvements of the MODIS
801 terrestrial gross and net primary production global data set. *Remote Sens. Environ.* **95**, 164–
802 176 (2005).

- 803 51. Larocque, G. R. *et al.* Process-Based Models: A Synthesis of Models and Applications to
804 Address Environmental and Management Issues. *Ecological Forest Management Handbook*
805 <https://www.taylorfrancis.com/> (2016) doi:10.1201/b19150-14.
- 806 52. Strigul, N., Pristinski, D., Purves, D., Dushoff, J. & Pacala, S. Scaling from Trees to
807 Forests: Tractable Macroscopic Equations for Forest Dynamics. *Ecol. Monogr.* **78**, 523–545
808 (2008).
- 809 53. Purves, D. & Pacala, S. Predictive Models of Forest Dynamics. *Science* **320**, 1452–1453
810 (2008).
- 811 54. Yang, Y., Zhu, Q., Peng, C., Wang, H. & Chen, H. From plant functional types to plant
812 functional traits: A new paradigm in modelling global vegetation dynamics. *Prog. Phys.*
813 *Geogr. Earth Environ.* **39**, 514–535 (2015).
- 814 55. Quillet, A., Peng, C. & Garneau, M. Toward dynamic global vegetation models for
815 simulating vegetation–climate interactions and feedbacks: recent developments, limitations,
816 and future challenges. *Environ. Rev.* **18**, 333–353 (2010).
- 817 56. Andes Biodiversity and Ecosystem Research Group | Using the Andes-Amazon gradient
818 as a laboratory for understanding global change. <http://www.andesconservation.org/>.
- 819 57. Malhi, Y. *et al.* The variation of productivity and its allocation along a tropical elevation
820 gradient: a whole carbon budget perspective. *New Phytol.* **214**, 1019–1032 (2017).
- 821 58. Asner, G. P., Martin, R. E., Anderson, C. B. & Knapp, D. E. Quantifying forest canopy
822 traits: Imaging spectroscopy versus field survey. *Remote Sens. Environ.* **158**, 15–27 (2015).
- 823 59. Asner, G. P. & Mascaro, J. Mapping tropical forest carbon: Calibrating plot estimates to a
824 simple LiDAR metric. *Remote Sens. Environ.* **140**, 614–624 (2014).

- 825 60. Asner, G. P. *et al.* A universal airborne LiDAR approach for tropical forest carbon
826 mapping. *Oecologia* **168**, 1147–1160 (2012).
- 827 61. Le Toan, T. *et al.* Relating Radar Remote Sensing of Biomass to Modelling of Forest
828 Carbon Budgets. *Clim. Change* **67**, 379–402 (2004).
- 829 62. Mascaro, J., Detto, M., Asner, G. P. & Muller-Landau, H. C. Evaluating uncertainty in
830 mapping forest carbon with airborne LiDAR. *Remote Sens. Environ.* **115**, 3770–3774 (2011).
- 831 63. Durán, S. M. *et al.* Informing trait-based ecology by assessing remotely sensed functional
832 diversity across a broad tropical temperature gradient. *Sci. Adv.* **5**, eaaw8114 (2019).
- 833 64. Karadimou, E. K., Kallimanis, A. S., Tsiripidis, I. & Dimopoulos, P. Functional diversity
834 exhibits a diverse relationship with area, even a decreasing one. *Sci. Rep.* **6**, 35420 (2016).
- 835 65. Schneider, F. D. *et al.* Mapping functional diversity from remotely sensed morphological
836 and physiological forest traits. *Nat. Commun.* **8**, 1441 (2017).
- 837 66. Caughlin, T. T. *et al.* A hyperspectral image can predict tropical tree growth rates in
838 single-species stands. *Ecol. Appl.* **26**, 2369–2375 (2016).
- 839 67. Lamanna, C. *et al.* Functional trait space and the latitudinal diversity gradient. *Proc. Natl.*
840 *Acad. Sci.* **111**, 13745–13750 (2014).
- 841 68. Chave, J. *et al.* Improved allometric models to estimate the aboveground biomass of
842 tropical trees. *Glob. Change Biol.* **20**, 3177–3190 (2014).
- 843 69. Drake, J. B., Dubayah, R. O., Knox, R. G., Clark, D. B. & Blair, J. B. Sensitivity of large-
844 footprint lidar to canopy structure and biomass in a neotropical rainforest. *Remote Sens.*
845 *Environ.* **81**, 378–392 (2002).

- 846 70. Valladares, F., Skillman, J. B. & Pearcy, R. W. Convergence in light capture efficiencies
847 among tropical forest understory plants with contrasting crown architectures: a case of
848 morphological compensation. *Am. J. Bot.* **89**, 1275–1284 (2002).
- 849 71. Asner, G.P. *et al.* The high-resolution carbon geography of Peru. (2014).
- 850 72. Martin, A. R. & Thomas, S. C. A Reassessment of Carbon Content in Tropical Trees.
851 *PLOS ONE* **6**, e23533 (2011).
- 852 73. Feldpausch, T. R. *et al.* Height-diameter allometry of tropical forest trees. *Biogeosciences*
853 **8**, 1081–1106 (2011).
- 854 74. R Core Team. R: A language and environment for statistical computing.
855

856 **Data availability**

857 The raw data that support the findings of this study were used under license from the Global
858 Airborne Observatory at Arizona State University, and so are not publicly available. Data
859 products (productivity estimates) and simulated raw data for use in productivity algorithms are
860 however available at Figshare (upon publication).

861

862 **Code availability**

863 All custom scripts used in this study are available on GitHub (upon publication).

864

865 **Author contributions**

866 All authors contributed to the design of the study. R.M. and G.P.A. collected the remote-sensing
867 data. D.J.W. and V.M.S. designed the models and D.J.W. performed all analyses. D.J.W.,
868 V.M.S. wrote the manuscript. All authors contributed to editing the manuscript.

869 **Supplementary Tables & Figures**

Plot (Elevation)	Plot-scale				Landscape-scale			
	Measured NPP	Ground (1ha)	RS-CFM (0.01ha)	RS-CFM (1ha)	RS-CFM (0.01ha)	RS-CFM (1ha)	RS-CFM (100ha)	MODIS (100ha)
TAM_06 (215m)	11.60	n = 1 12.18 (0.58)	n = 600 12.29 ± 2.67 (0.69)	n = 8 10.24 ± 0.9 (-1.36)	n = 86711 14.31 ± 2.81 (2.71)	n = 1038 12.31 ± 1.07 (0.71)	n = 32 11.64 ± 0.62 (0.04)	n = 45 18.9 ± 0.22 (7.3)
TAM_05 (223m)	14.28	n = 1 13.85 (-0.43)	n = 853 14.31 ± 2.38 (0.03)	n = 9 13.04 ± 0.67 (-1.24)	n = 46067 14.11 ± 2.89 (-0.17)	n = 524 13.06 ± 0.9 (-1.22)	n = 6 12.39 ± 0.27 (-1.89)	n = 21 18.73 ± 0.3 (4.45)
PAN_02 (595m)	11.34	n = 1 12.05 (0.71)	n = 871 12.82 ± 1.79 (1.48)	n = 9 10.66 ± 0.23 (-0.68)	n = 35984 14.31 ± 2.74 (2.97)	n = 562 13.42 ± 1.6 (2.08)	n = 17 11.18 ± 0.56 (-0.16)	n = 17 18.14 ± 2.97 (6.8)
SPD_02 (1527m)	12.08	n = 1 9.33 (-2.75)	n = 704 13.17 ± 2.79 (1.09)	n = 9 10.54 ± 0.81 (-1.54)	n = 465340 11.66 ± 3.65 (-0.42)	n = 9667 10.62 ± 2.88 (-1.46)	n = 192 8.6 ± 1.7 (-3.48)	n = 334 20.18 ± 2.13 (8.1)
SPD_01 (1776m)	8.01	n = 1 9.33 (1.32)	n = 470 7.1 ± 1.85 (-0.91)	n = 9 5.51 ± 0.75 (-2.5)	n = 168747 8.95 ± 2.33 (0.94)	n = 3874 8.11 ± 2 (0.1)	n = 131 7.29 ± 1.65 (-0.72)	n = 252 19.96 ± 2.55 (11.95)
TRU_04 (2758m)	7.77	n = 1 7.55 (-0.22)	n = 656 7.65 ± 1.89 (-0.12)	n = 9 6.39 ± 0.5 (-1.38)	n = 303322 7.93 ± 2.71 (0.16)	n = 6046 7.03 ± 2.05 (-0.74)	n = 140 5.07 ± 0.87 (-2.7)	n = 313 18.7 ± 4.37 (10.93)
ESP_01 (2863m)	7.73	n = 1 8.38 (0.65)	n = 353 8.5 ± 3 (0.77)	n = 6 6.48 ± 1.47 (-1.25)	n = 180731 9.39 ± 3.56 (1.66)	n = 3589 8.08 ± 2.5 (0.35)	n = 42 6.64 ± 1.19 (-1.09)	n = 285 17.88 ± 4.76 (10.15)
WAY_01 (3045m)	7.86	n = 1 7.26 (-0.6)	n = 591 6.08 ± 1.85 (-1.78)	n = 9 5.31 ± 0.78 (-2.55)	n = 178440 9.1 ± 3.47 (1.24)	n = 4210 7.9 ± 2.48 (0.04)	n = 109 6.52 ± 1.5 (-1.34)	n = 288 16.19 ± 5.76 (8.33)
ACJ_01 (3537m)	7.89	n = 1 9.8 (1.91)	n = 197 8.85 ± 1.71 (0.96)	n = 6 7.45 ± 0.22 (-0.44)	n = 12913 10.07 ± 3.19 (2.18)	n = 530 9.08 ± 2.59 (1.19)	n = 41 7.58 ± 1.31 (-0.31)	n = 154 9.29 ± 5.52 (1.4)
Across all elevations	n = 9 9.84 ± 2.5 (n/a)	n = 9 9.97 ± 2.26 (0.13 ± 1.35)	n = 5295 10.71 ± 3.77 (0.26 ± 2.47)	n = 74 8.49 ± 2.79 (-1.49 ± 0.98)	n = 1478255 10.28 ± 3.78 (0.61 ± 3.36)	n = 30040 9.01 ± 2.98 (-0.5 ± 2.56)	n = 710 7.4 ± 2.23 (-1.91 ± 1.87)	n = 1709 17.77 ± 5.14 (8.88 ± 5.05)
RMSD	n/a	1.28	1.02	1.59	1.71	1.08	1.72	8.31

870

871 **Table S1.** Empirical NPP measurements and a summary of ground-based and RS-CFM model
872 pixel growth rate estimates within and across all plots/elevations shown at multiple spatial scales
873 (plot and landscape) and resolutions (0.01ha, 1ha, and 100ha). NPP units are standardized to
874 MgC ha⁻¹ yr⁻¹ for all scales and resolutions. For each table entry, the first line (n) designates
875 number of samples (pixels), the second line shows mean ± standard deviation of \dot{M}_{pixel} values,
876 and the third line shows mean pixel growth rate deviations ($\dot{M}_{pixel} - \text{measured NPP}$) in

877 parentheses. For across-elevation entries, the third line also provides standard deviations in pixel
 878 growth rate deviations.

879

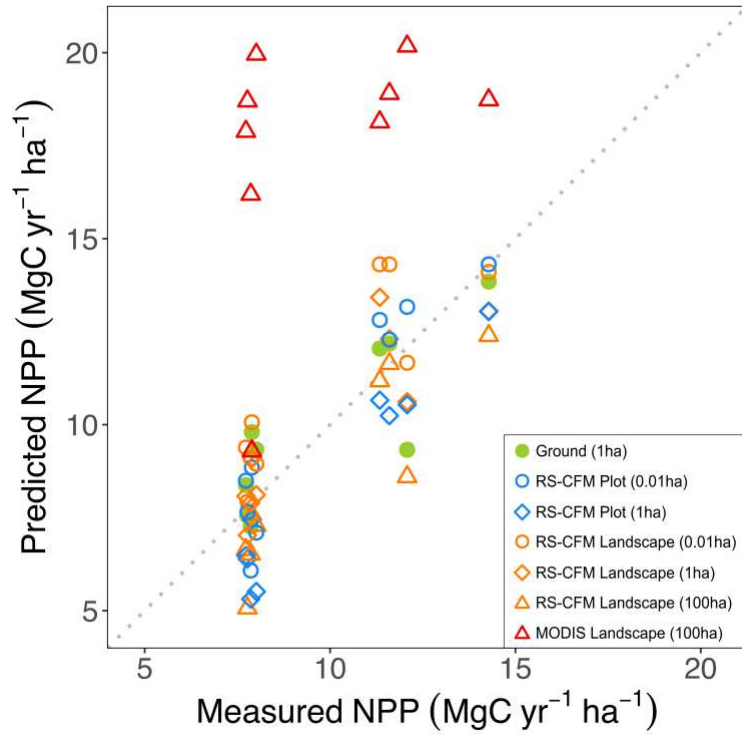
Scale	Resolution	Parameter	Estimate	Std. Error	T-value	p-value	
Plot	0.01ha adj. R2 = 0.916 p < 10 ⁻⁵	Intercept	10.708	0.015	711.82	<10 ⁻⁵	
		LMA	-2.032	0.025	-82.946	<10 ⁻⁵	
		N _{area}	0.065	0.023	2.805	0.00505	
		P _{area}	0.232	0.028	8.324	<10 ⁻⁵	
		A _L	2.692	0.04	67.535	<10 ⁻⁵	
		M _L	2.466	0.027	89.972	<10 ⁻⁵	
	1ha adj. R2 = 0.962 p < 10 ⁻⁵	Intercept	8.494	0.064	133.522	<10 ⁻⁵	
		LMA	-1.571	0.117	-13.416	<10 ⁻⁵	
		N _{area}	-0.099	0.109	-0.913	0.36465	
		P _{area}	0.298	0.098	3.034	0.00342	
		A _L	1.94	0.107	18.208	<10 ⁻⁵	
		M _L	1.555	0.094	16.473	<10 ⁻⁵	
	Landscape	0.01ha adj. R2 = 0.885 p < 10 ⁻⁵	Intercept	10.281	0.001	9760.3	<10 ⁻⁵
			LMA	-1.81	0.001	-1484.464	<10 ⁻⁵
			N _{area}	0.26	0.002	154.967	<10 ⁻⁵
P _{area}			0.335	0.002	172.008	<10 ⁻⁵	
A _L			3.166	0.003	987.694	<10 ⁻⁵	
M _L			3.423	0.002	1716.488	<10 ⁻⁵	
1ha adj. R2 = 0.899 p < 10 ⁻⁵		Intercept	9.014	0.005	1648.078	<10 ⁻⁵	
		LMA	-1.446	0.006	-235.41	<10 ⁻⁵	
		N _{area}	0.066	0.009	7.26	<10 ⁻⁵	
		P _{area}	0.137	0.01	13.737	<10 ⁻⁵	
		A _L	2.356	0.017	140.773	<10 ⁻⁵	
		M _L	2.414	0.01	231.569	<10 ⁻⁵	
100ha adj. R2 = 0.909 p < 10 ⁻⁵		Intercept	7.397	0.025	292.745	<10 ⁻⁵	
		LMA	-1.132	0.029	-38.4	<10 ⁻⁵	
		N _{area}	-0.228	0.039	-5.858	<10 ⁻⁵	
		P _{area}	-0.222	0.036	-6.25	<10 ⁻⁵	
		A _L	1.48	0.067	22.088	<10 ⁻⁵	
		M _L	1.279	0.05	25.351	<10 ⁻⁵	

880

881 **Table S2.** Multiple regression summary showing the effects of individual model components on

882 RS-CFM pixel growth rate estimates (\dot{M}_{pixel}). Regression coefficient estimates are standardized

883 to allow comparison of effect sizes among model components.



884

885 **Figure S1.** Deviations between measured and predicted (model) NPP estimates.

886

887

888

889

890

891

892

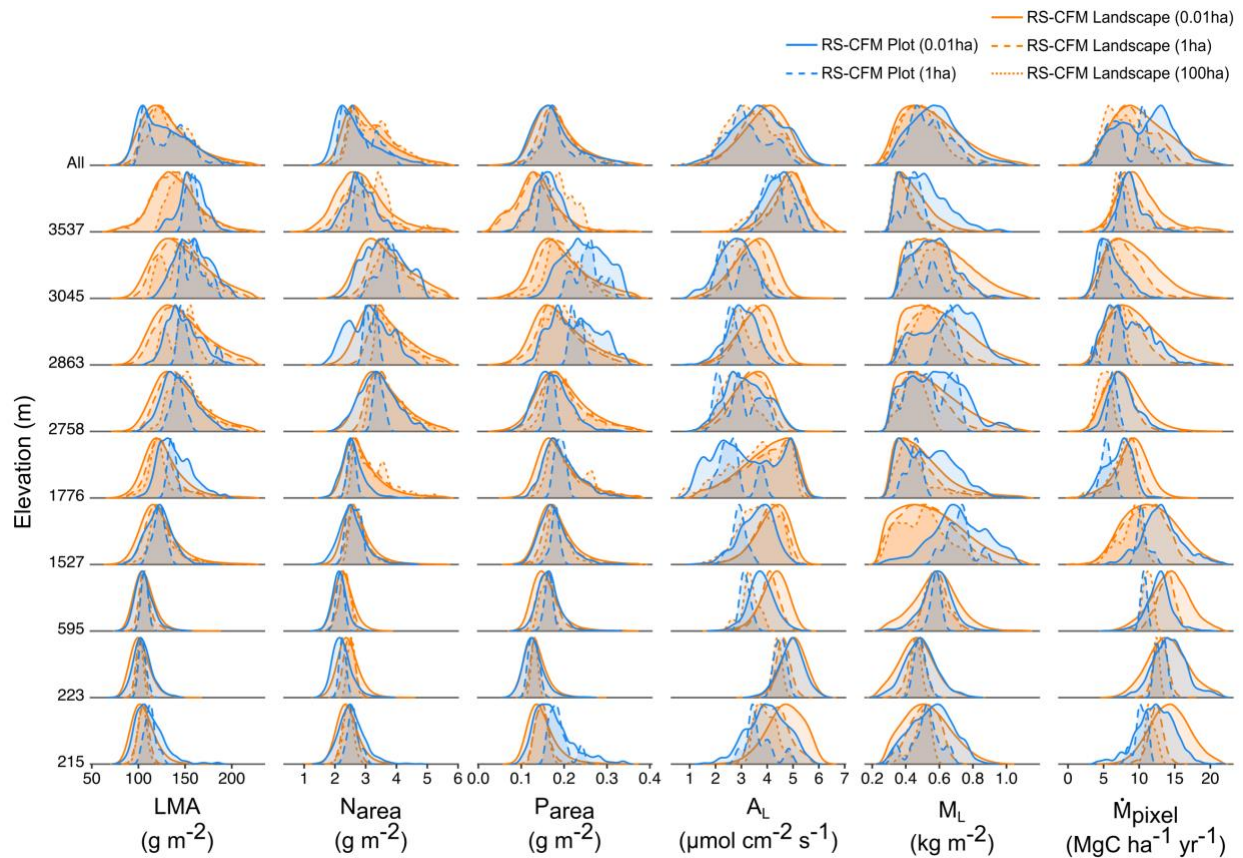
893

894

895

896

897



898

899 **Figure S2.** Distributions of individual model components and \dot{M}_{pixel} estimates within and across
 900 elevations shown at multiple spatial scales (plot and landscape) and resolutions (0.01ha, 1ha, and
 901 100ha). Plot- and landscape-scale data cover a total of 81 and 30,040 hectares, respectively.
 902 Variables are leaf mass per unit area (LMA), area-based leaf nitrogen (N_{area}) and phosphorus
 903 (P_{area}) content, leaf photosynthetic rate (A_L), total pixel leaf biomass (M_L), and pixel vegetation
 904 growth rate (\dot{M}_{pixel}).

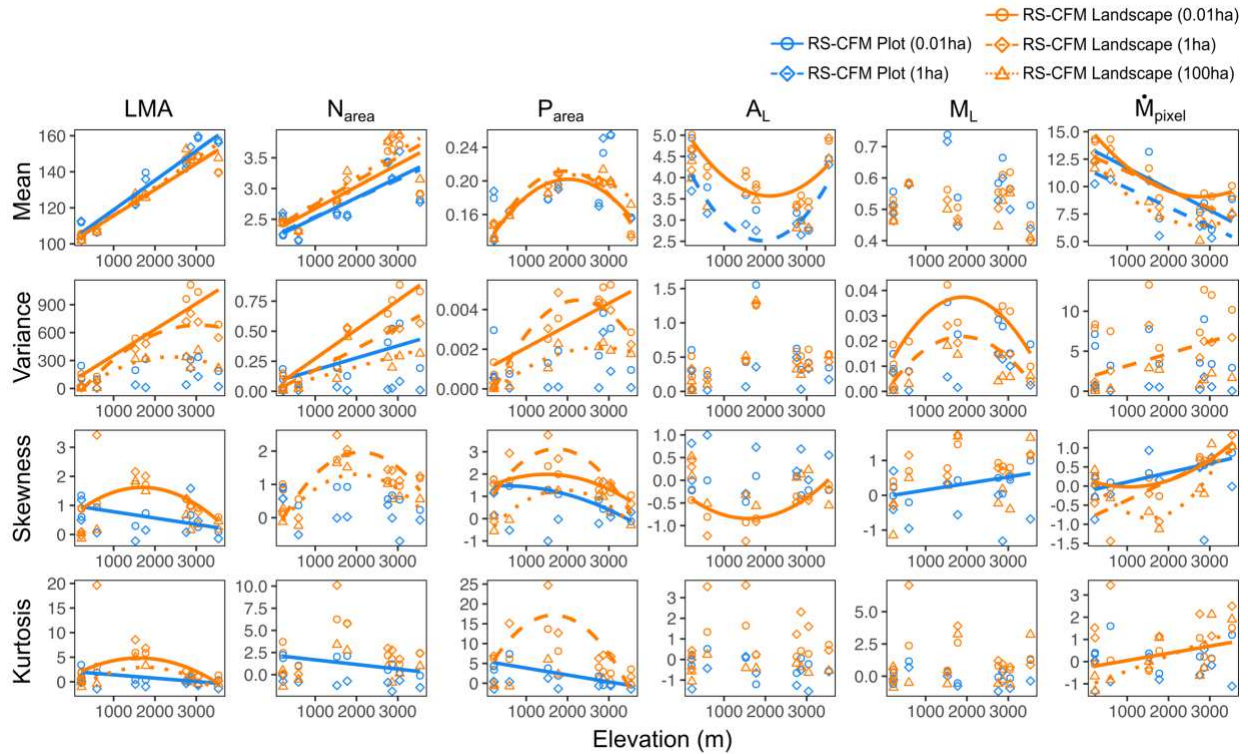
905

906

907

908

909



910

911 **Figure S3.** Trends in moments of the distributions of individual model components and \dot{M}_{pixel}
 912 estimates across elevations shown at multiple spatial scales (plot and landscape) and resolutions
 913 (0.01ha, 1ha, and 100ha). Lines designate significant regressions. Both linear and quadratic
 914 regressions were tested—linear model fits are shown for cases where both linear and quadratic
 915 models produced significant fits and AIC scores differed by less than 4 points. Traits are leaf
 916 mass per unit area (LMA), area-based leaf nitrogen (N_{area}) and phosphorus (P_{area}) content, leaf
 917 photosynthetic rate (A_L), total pixel leaf biomass (M_L), and pixel vegetation growth rate (\dot{M}_{pixel}).

918

Figures

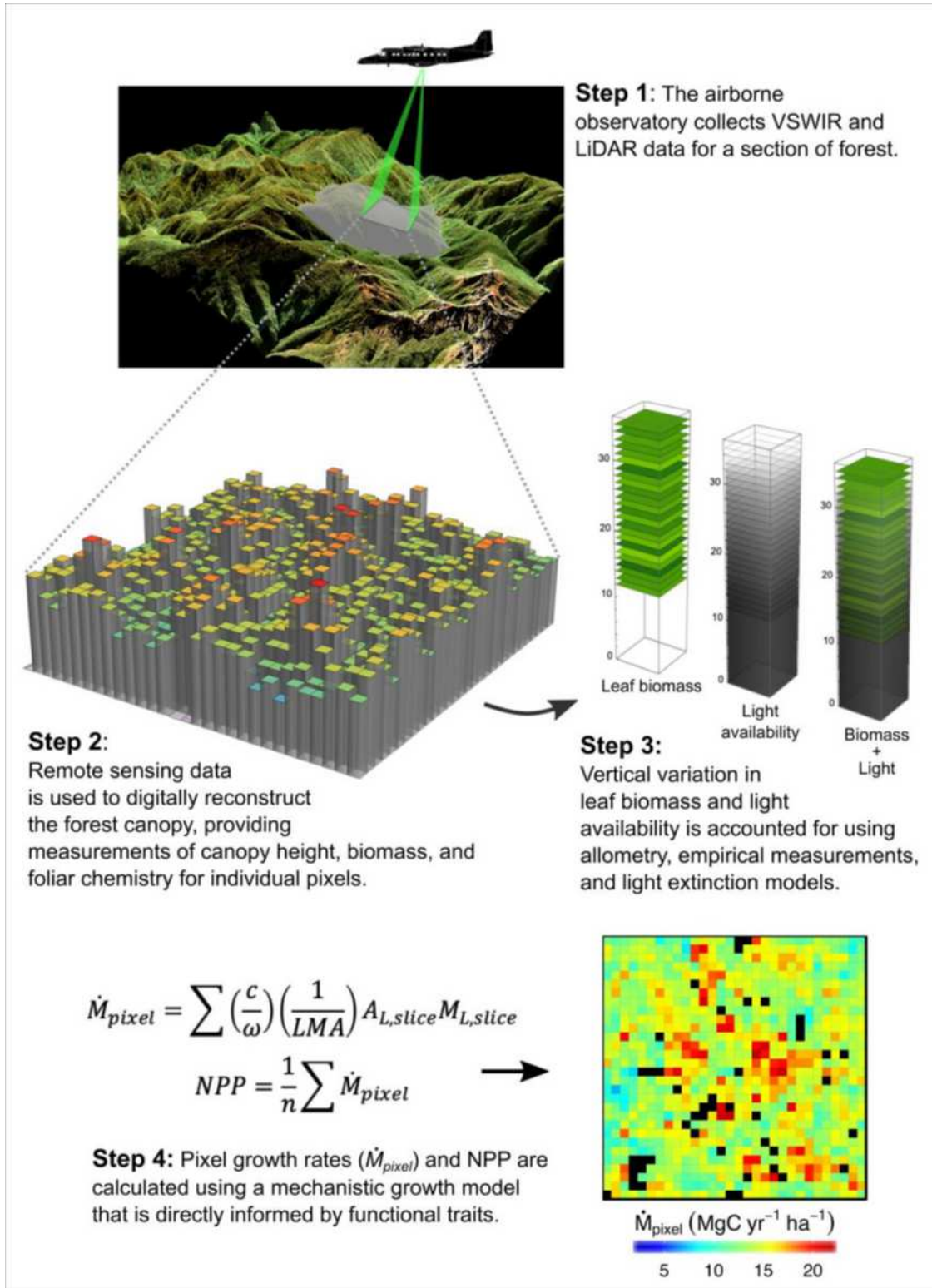


Figure 1

Step-by-step process for converting remote sensing data into productivity estimates using our trait-based remote sensing canopy functional model (RS-CFM) framework.

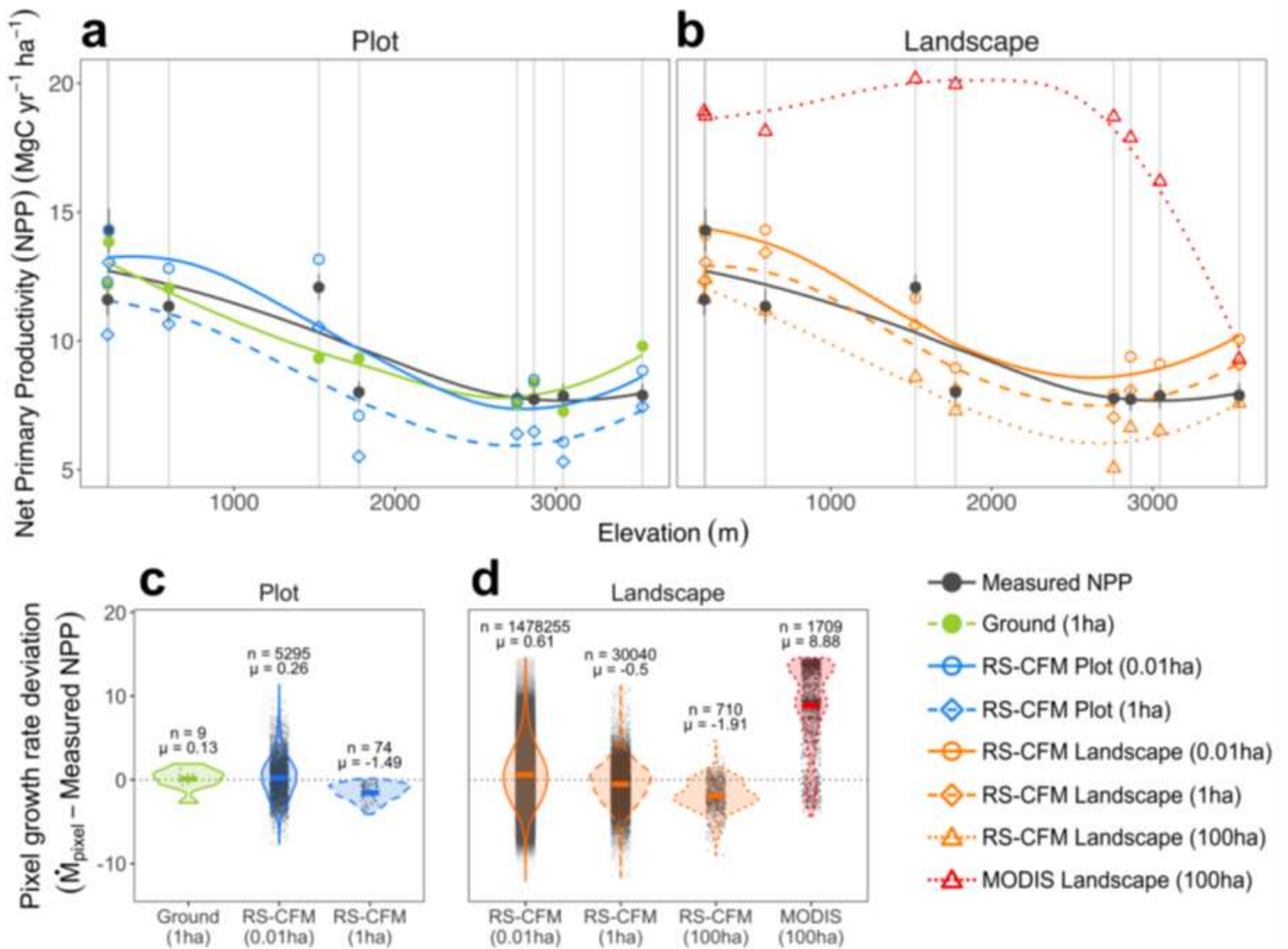


Figure 2

(a-b) Net primary productivity (NPP) and (c-d) individual pixel vegetation growth rate estimates (\dot{M}_{pixel}) from ground-based, airborne remote sensing (RS-CFM), and NASA-MODIS NPP models shown at multiple spatial scales (plot and landscape) and resolutions (0.01ha, 1ha, and 100ha).

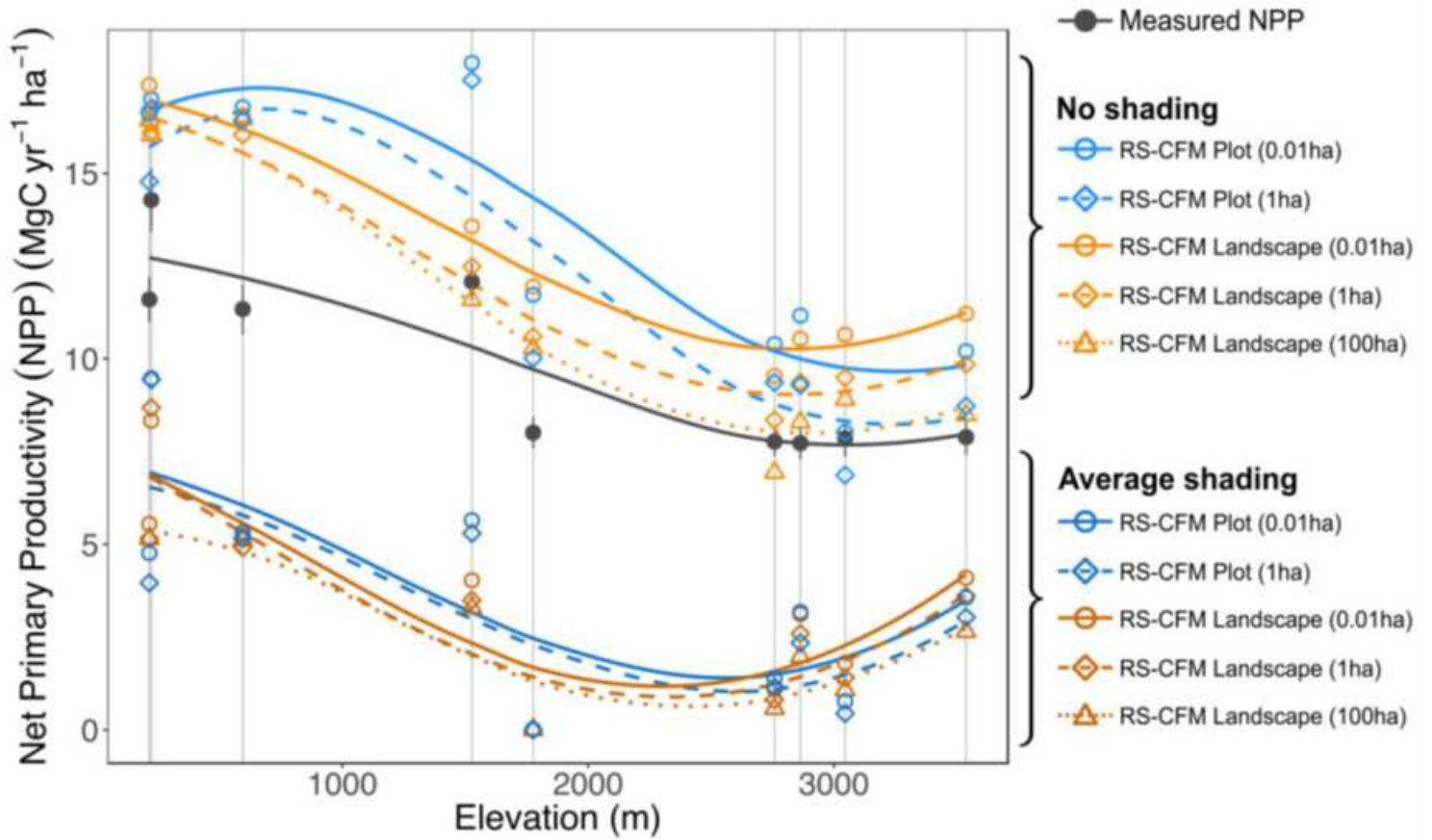


Figure 3

Remote sensing productivity estimates (RS-CFM) calculated using alternative canopy shading schemes. “No shading” indicates that light is freely available throughout the canopy and “Average shading” indicates that each vertical canopy slice receives the same amount of light equal to the average throughout a given pixel.

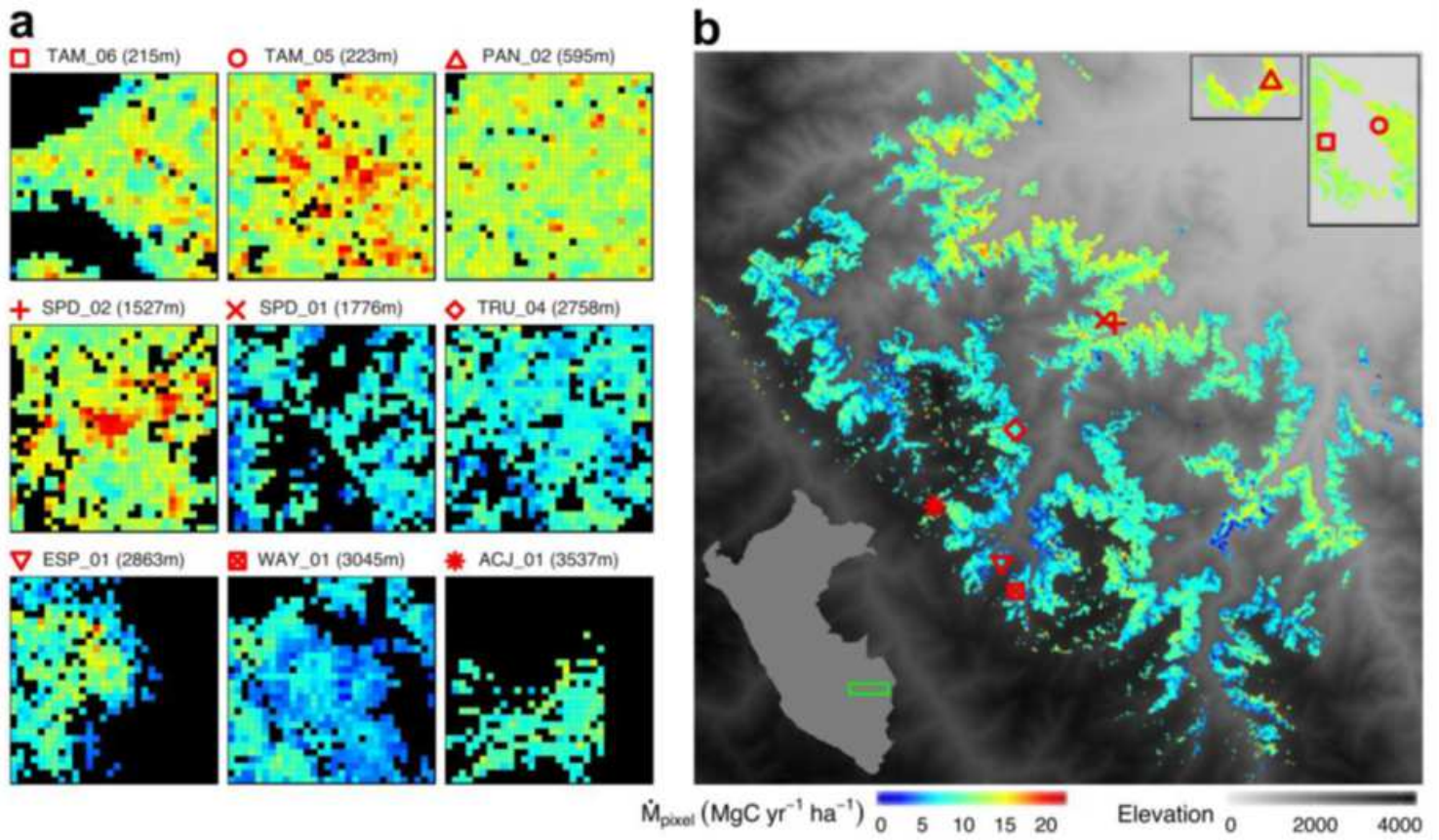


Figure 4

Spatial maps of landscape-scale growth estimates for individual pixels (\dot{M}_{pixel}) using our remote sensing canopy functional model (RS-CFM) at (a) 0.01ha resolution for individual forest plots and (b) 1ha-resolution for 30,040 hectares of forest surrounding the nine focal plots. Boxes in the upper right corner show areas outside the main plot area. Black pixels in plot-level images are no data values.